iScience

CellPress
OPEN ACCESS

Article

Histone deacetylation regulates nucleotide excision repair through an interaction with the XPC protein

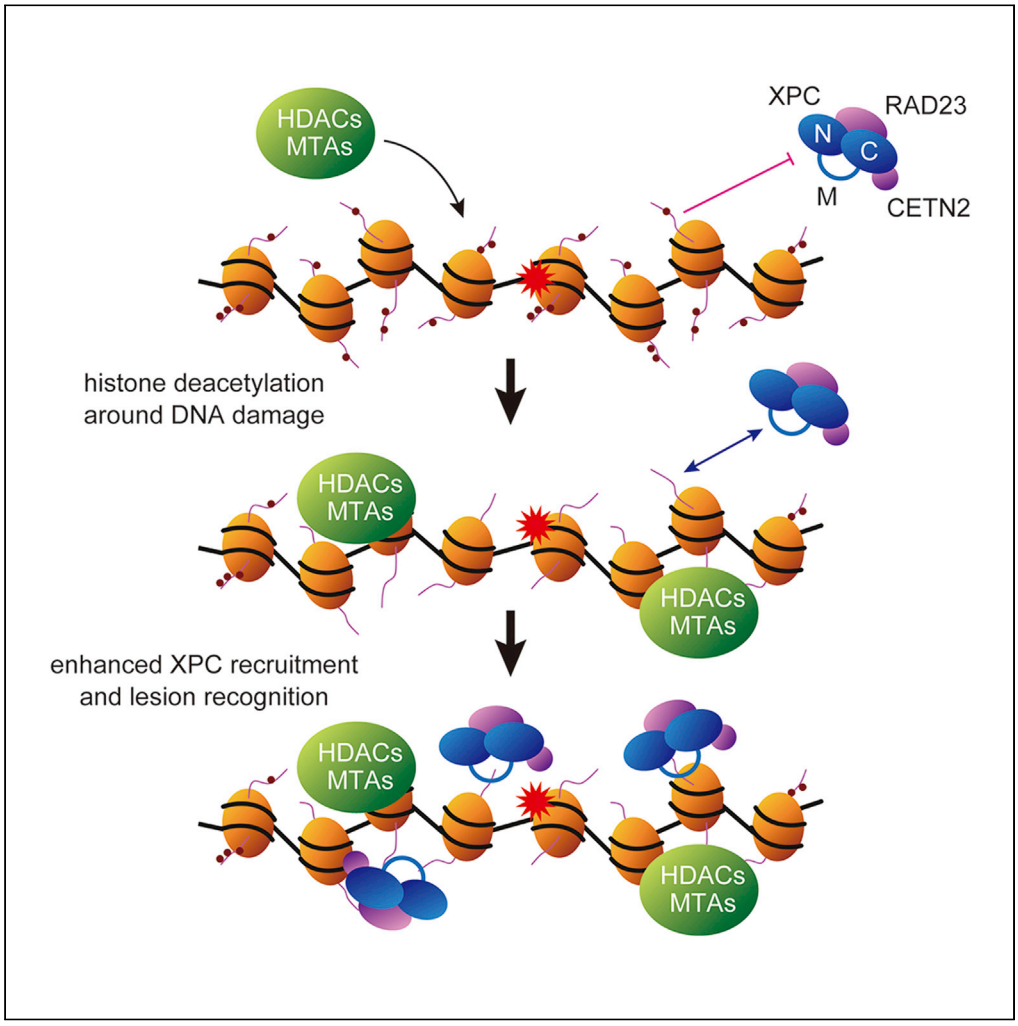

Masayuki Kusakabe, Erina Kakumu, Fumika Kurihara, ..., Masayuki Yokoi, Wataru Sakai, Kaoru Sugasawa

ksugasawa@garnet.kobe-u.ac.jp

Highlights

Histone deacetylation by HDAC1/2 promotes the DNA lesion recognition by XPC

The HDAC1/2 activators, MTA proteins, also promote the recruitment of XPC

XPC tends to localize in hypoacetylated chromatin independently of DNA damage

Disordered middle region of XPC interacts with histone H3 tail and promotes GG-NER

Kusakabe et al., iScience 25, 104040
April 15, 2022
https://doi.org/10.1016/j.isci.2022.104040

iScience

CellPress
OPEN ACCESS

Article

Histone deacetylation regulates nucleotide excision repair through an interaction with the XPC protein

Masayuki Kusakabe,[1] Erina Kakumu,[1,2] Fumika Kurihara,[1,2] Kazuki Tsuchida,[1,2] Takumi Maeda,[1,2] Haruto Tada,[1,2] Kanako Kusao,[1,2] Akari Kato,[1,2] Takeshi Yasuda,[3] Tomonari Matsuda,[4] Mitsuyoshi Nakao,[5] Masayuki Yokoi,[1,2] Wataru Sakai,[1,2] and Kaoru Sugasawa[1,2,6,*]

SUMMARY

The XPC protein complex plays a central role in DNA lesion recognition for global genome nucleotide excision repair (GG-NER). Lesion recognition can be accomplished in either a UV-DDB-dependent or -independent manner; however, it is unclear how these sub-pathways are regulated in chromatin. Here, we show that histone deacetylases 1 and 2 facilitate UV-DDB-independent recruitment of XPC to DNA damage by inducing histone deacetylation. XPC localizes to hypoacetylated chromatin domains in a DNA damage-independent manner, mediated by its structurally disordered middle (M) region. The M region interacts directly with the N-terminal tail of histone H3, an interaction compromised by H3 acetylation. Although the M region is dispensable for *in vitro* NER, it promotes DNA damage removal by GG-NER *in vivo*, particularly in the absence of UV-DDB. We propose that histone deacetylation around DNA damage facilitates the recruitment of XPC through the M region, contributing to efficient lesion recognition and initiation of GG-NER.

INTRODUCTION

Genomic DNA is highly susceptible to damage caused by a variety of endogenous and environmental stresses. Such DNA damage, if left unrepaired, can interfere with fundamental cellular processes, such as transcription, replication, and chromosome segregation, provoking genome instability and cell death. To minimize these deleterious effects, it is crucial for organisms to detect and remove the DNA lesions efficiently.

Nucleotide excision repair (NER) is a major DNA repair pathway for the elimination of a wide variety of helix-distorting DNA lesions (Schärer, 2013), including DNA photolesions induced by ultraviolet light (UV), such as cyclobutane pyrimidine dimers (CPDs) and pyrimidine (6–4) pyrimidone photoproducts (6-4PPs), intrastrand crosslinks induced by divalent chemical compounds (e.g., cisplatin), and bulky base adducts induced by chemical carcinogens (Gillet and Schärer, 2006). In humans, hereditary defects in NER are associated with several autosomal disorders, such as xeroderma pigmentosum (XP), which is clinically characterized by hypersensitivity to UV and an increased predisposition to skin cancers. Seven NER-deficient XP complementation groups (XP-A through G) have been identified, and the functions of XP gene products in NER are well understood (DiGiovanna and Kraemer, 2012; Nishigori and Sugasawa, 2019).

Lesion recognition is a key step affecting the efficiency of DNA repair. In eukaryotes, DNA lesions are processed through one of two sub-pathways: global genome NER (GG-NER), which acts upon whole genome, and transcription-coupled NER (TC-NER), which specifically removes lesions from actively transcribed DNA strands (Marteijn et al., 2014). A DNA-binding protein complex containing one XP-related gene product, XPC (XPC-RAD23-CETN2 heterotrimer), plays a central role in the recognition of DNA lesions during GG-NER (Riedl et al., 2003; Sugasawa et al., 1998; Volker et al., 2001). This complex binds specifically to double-stranded DNA, interacting with intact bases around the lesion that cannot conduct Watson–Crick base pairing, rather than with the lesion itself (Chen et al., 2015; Min and Pavletich, 2007;

[1]Biosignal Research Center, Kobe University, Kobe 657-8501, Japan

[2]Graduate School of Science, Kobe University, Kobe 657-8501, Japan

[3]Institute for Quantum Life Science, National Institutes for Quantum Science and Technology, Chiba 263-8555, Japan

[4]Research Center for Environmental Quality Management, Graduate School of Engineering, Kyoto University, Otsu 520-0811, Japan

[5]Institute of Molecular Embryology and Genetics, Kumamoto University, Kumamoto 860-0811, Japan

[6]Lead contact

*Correspondence: ksugasawa@garnet.kobe-u.ac.jp

https://doi.org/10.1016/j.isci.2022.104040

Sugasawa et al., 2002). Therefore, XPC is able to recognize and bind to sites of DNA damage in which the lesion induces large helical distortions (Sugasawa, 2019). While XPC is indispensable for the initiation of GG-NER, some organisms, including humans, can also utilize another damage recognition factor, DDB1-DDB2 (also known as UV-damaged DNA-binding protein [UV-DDB]), which is deficient in XP-E (Chu and Chang, 1988; Keeney et al., 1993; Rapić-Otrin et al., 2003). UV-DDB preferentially binds to UV-damaged DNA, interacting directly with photolesions (Fujiwara et al., 1999; Reardon et al., 1993; Scrima et al., 2008; Wittschieben et al., 2005), promoting the recruitment of XPC (Fitch et al., 2003; Moser et al., 2005; Nishi et al., 2009; Wang et al., 2004). This UV-DDB-mediated lesion recognition is particularly important for the efficient repair of CPDs (Hwang et al., 1999; Tang et al., 2000), which can escape detection by XPC as they induce relatively small helical distortions (Kusumoto et al., 2001; Sugasawa et al., 2001). By contrast, 6-4PPs can be recognized by either XPC or UV-DDB and, therefore, 6-4PP repair defects in XP-E cells are much less pronounced than in CPDs (Hwang et al., 1999; Tang et al., 2000). Chemically induced base lesions are supposed to be processed mostly by the UV-DDB-independent lesion recognition mechanism (Payne and Chu, 1994; Scrima et al., 2008).

Although the interactions of XPC and UV-DDB with DNA damage are well characterized biochemically and at an atomic resolution, the molecular mechanisms underlying the regulation of lesion recognition *in vivo* remain elusive (Polo and Almouzni, 2015). It has been established that various genomic functions in eukaryotes are regulated by the interconversion of chromatin structures, involving post-translational modifications of histones, DNA methylation, and chromatin remodeling. DNA lesion recognition is also under the control of chromatin, and various chromatin-related factors have been shown to be involved in GG-NER. For instance, UV-DDB interacts with histone acetyltransferases (Datta et al., 2001; Martinez et al., 2001; Matsunuma et al., 2016; Rapić-Otrin et al., 2002), histone deacetylases (HDACs) (Zhao et al., 2014; Zhu et al., 2015), and poly(ADP-ribose) polymerase 1 (PARP1) (Pines et al., 2012; Robu et al., 2013). Moreover, UV-DDB is part of a ubiquitin E3 ligase complex containing Cullin4-RBX1 (Fischer et al., 2011; Groisman et al., 2003), which is activated upon binding to UV-damaged DNA and ubiquitylates histones, XPC, and DDB2 (Kapetanaki et al., 2006; Sugasawa et al., 2005; Wang et al., 2006). Local chromatin structures bound by UV-DDB undergo remarkable decompaction (Adam et al., 2016; Luijsterburg et al., 2012), and it is likely that such alterations are advantageous for the recruitment of XPC during UV-DDB-dependent lesion recognition. Conversely, XPC can recognize and bind to 6-4PPs and to chemically induced base adducts, without the aid of UV-DDB (Batty et al., 2000; Sugasawa et al., 2001; Trego and Turchi, 2006), though it remains elusive how chromatin structure regulates the UV-DDB-independent lesion recognition by XPC.

In a previous study (Kakumu et al., 2017), we presented evidence to suggest that histone deacetylation plays a role in the regulation of DNA lesion recognition by XPC since 1) some acetylated histones were underrepresented in XPC-bound chromatin; 2) local UVC irradiation within the nucleus reduced the levels of acetylated histones in the damaged area; 3) treatment of cells with HDAC inhibitors partially compromised the recruitment of XPC to DNA damage and the removal of 6-4PPs; and 4) XPC directly interacted with histone H3, an interaction abrogated by acetylation of the histone protein. Based on these findings, we proposed that DNA lesions may induce alterations, including histone deacetylation, in nearby chromatin, and that such local chromatin environments may enhance the efficiency of lesion recognition, presumably by increasing the local concentration of XPC. However, it is unclear which lesion recognition pathway, UV-DDB-dependent or -independent, is regulated by this mechanism; which HDAC species is involved; or how histone deacetylation is regulated in response to DNA damage. Here, we further examine the roles of HDACs in the regulation of GG-NER, focusing on UV-DDB-independent lesion recognition by XPC. Our results provide a novel insight into chromatin regulation, which assists in the efficient repair of "difficult to detect" DNA lesions.

RESULTS

HDAC regulates DNA damage recognition by XPC

To examine in detail the involvement of HDACs in lesion recognition during GG-NER, we used a live cell imaging system combined with local UVC stimulation. This system enabled the quantitative monitoring of the recruitment of fluorescently labeled proteins to UV-induced DNA photolesions in real time (Meldrum et al., 2003; Sakai et al., 2020). To focus on the UV-DDB-independent lesion recognition sub-pathway, endogenous *DDB2* was disrupted in U2OS cells that stably express EGFP-tagged XPC (Figure S1A). In these cells, EGFP-XPC was expressed at a substantially higher level than endogenous XPC. Upon treatment

with the pan-HDAC inhibitor trichostatin A (TSA) or the class I HDAC-specific inhibitor romidepsin, the accumulation of EGFP-XPC to local UV damage (LUD) was compromised in a dose-dependent manner (Figures 1A, 1B, S1B, S1C, and S1D). We confirmed that the overall expression level of EGFP-XPC was not significantly affected by treatment with these HDAC inhibitors (Figure S1E). In addition, fluorescence recovery after photobleaching (FRAP) analyses indicated that the observed effect of HDAC inhibitors on EGFP-XPC accumulation was not attributed to reduced mobility of EGFP-XPC within the nucleus (Figures S1F–S1H). Therefore, these results indicate that class I HDACs are involved in the regulation of DNA lesion recognition by XPC.

To determine the HDAC species responsible, expression of class I HDACs (HDAC1, 2, 3, and 8) was individually suppressed (Figure 1C). Notably, depletion of HDAC2 compromised the recruitment of EGFP-XPC, whereas suppression of HDAC1, 3, or 8 had little effect (Figures 1D and S2A). Similar result was obtained with a different siRNA targeting HDAC2 (Figure S2B). Consistent with the effects of HDAC inhibitors, neither the expression level nor the mobility of EGFP-XPC was significantly affected by the suppression of HDAC2 or any other class I HDACs (Figures S2C and S2D).

Next, we addressed whether HDAC2 was involved in the deacetylation of histone proteins at sites of UV-induced DNA damage. Consistent with our previous work (Kakumu et al., 2017), the level of Lys27-acetylated histone H3 (H3K27ac) was significantly reduced at LUD sites after UVC irradiation through isopore membrane filters in our *DDB2*-deficient U2OS cells (Figures S3A and S3B). Notably, the reduced H3K27ac staining was not attributed to the decreased density of histone H3 *per se* (Figures S3A and S3C), supporting the notion that the deacetylation of histone H3 occurred at LUD sites. When HDAC2 was depleted by siRNA, the suppression of H3K27ac was alleviated (Figure 1E). By contrast, suppression of any other class I HDACs did not significantly affect H3K27ac levels. Collectively, these results strongly suggest that HDAC2 induces histone deacetylation at sites of DNA damage, which facilitates the recruitment of XPC in a UV-DDB-independent manner.

HDAC1 and HDAC2 have redundant functions in XPC recruitment

Although HDAC1 and HDAC2 are thought to have overlapping functions, depletion of HDAC1 did not affect XPC recruitment or histone deacetylation at LUD sites (Figures 1D, 1E, and S2A). By using transiently expressed EGFP-tagged HDAC1 and HDAC2 as internal controls, we found that the level of endogenous HDAC1 is approximately 3.7 times lower than that of HDAC2 in our *DDB2*-deficient U2OS cells (Figure S4A). Notably, stable overexpression of hemagglutinin (HA)-tagged HDAC1 (HDAC1-HA) resulted in the suppression of endogenous HDAC2, while the negative effects of HDAC2 depletion on XPC recruitment could be counteracted by overexpressing HDAC1 (Figures S4B and S4C). Therefore, we conclude that HDAC1 and HDAC2 have redundant functions in the regulation of GG-NER, and the apparent difference in response following siRNA was likely due to the different expression levels of these HDAC species.

We next addressed the role of HDAC catalytic activity in the accumulation of EGFP-XPC to LUD sites. To this end, we prepared the siRNA-resistant version of HDAC2, either wild type or mutant harboring a His142Ala substitution (Hassig et al., 1998), which was fused to the N-terminus of HaloTag 7 (HDAC2-Halo) (Figure S4D). When these HDAC2-Halo proteins were expressed in HDAC2-depleted cells, we unexpectedly observed that both wild-type and mutant HDAC2 similarly restored the accumulation of EGFP-XPC (data not shown). HDAC1 and HDAC2 are known as components of transcriptional corepressors, such as the nucleosome-remodeling and deacetylase (NuRD) complex (Xue et al., 1998; Zhang et al., 1997, 1999), in which two HDAC1/2 molecules are present. Therefore, it was conceivable that, when expressed in HDAC2-depleted cells, mutant HDAC2 could interact with endogenous HDAC1 and consequently increase the number of catalytically active complexes. Based on such consideration, we decided to deplete both HDAC1 and HDAC2. Like the depletion of HDAC2 alone (Figure 1C), the accumulation of EGFP-XPC upon local UVC stimulation was compromised by the simultaneous suppression of HDAC1/2 (Figures S4E and S4F). The reduction in XPC accumulation was counteracted by the expression of siRNA-resistant wild-type HDAC2, whereas this rescue was abolished by the H142A mutation. Taken together, we conclude that HDAC1/2 promotes XPC recruitment to sites of DNA damage depending on their catalytic activities.

HDAC2 accumulates at LUD sites

The data above suggest that HDAC2 is recruited to DNA damage and induces the deacetylation of histones in the vicinity. This hypothesis was addressed with *DDB2*-deficient U2OS cells ectopically expressing

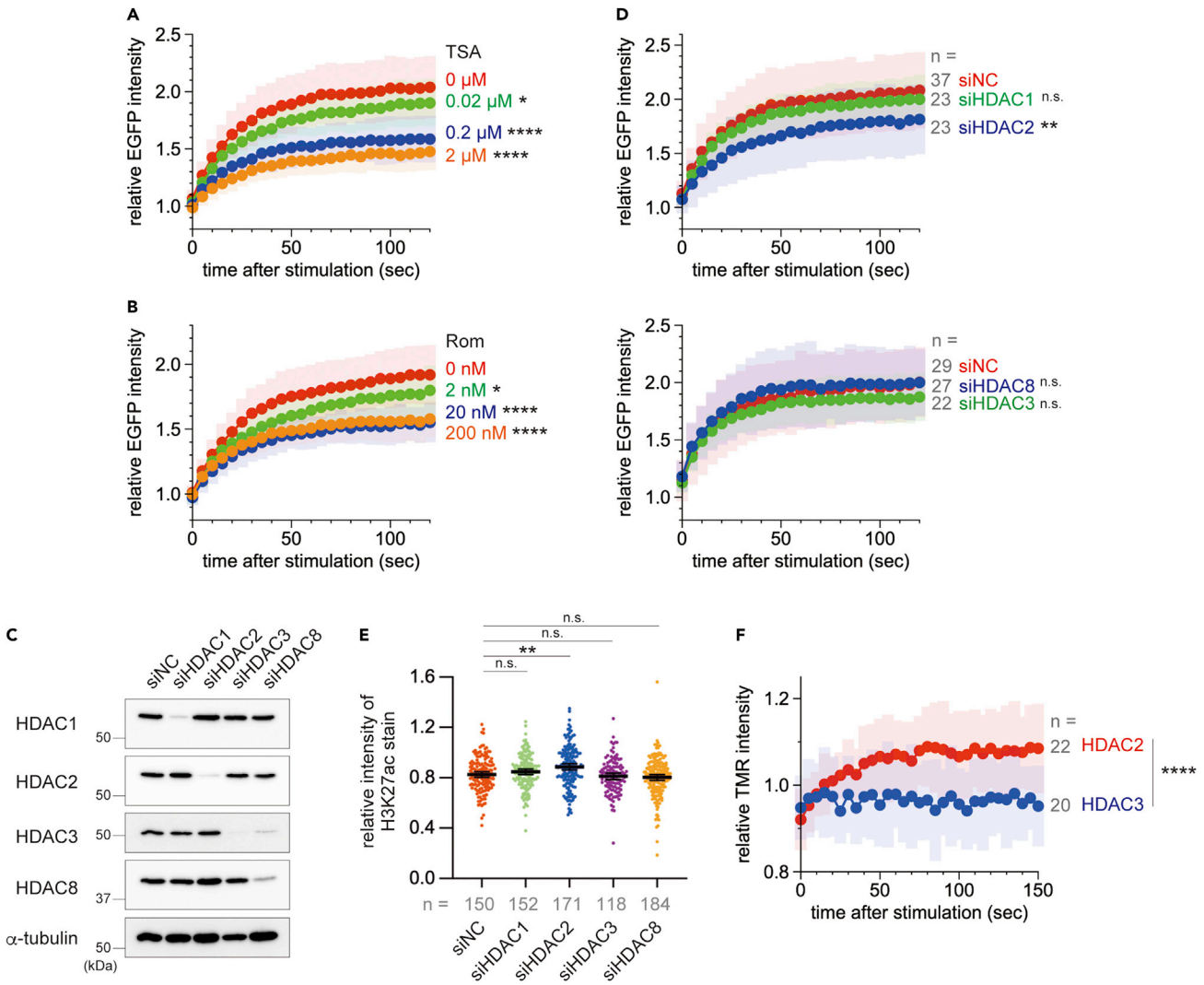

Figure 1. Roles for HDACs in UV-DDB-independent DNA lesion recognition by XPC

(A and B) *DDB2*-deficient U2OS cells stably expressing EGFP-XPC were pre-treated for 6 h with various concentrations of TSA (A) or romidepsin (B). Local UVC stimulation was applied, and the accumulation of EGFP-XPC to LUD sites was monitored by time-lapse imaging. The EGFP intensity in each stimulated area relative to the entire nucleus was calculated and plotted as described previously (Sakai et al., 2020). The graphs show the mean and SDs at individual time points (32 cells were analyzed for each condition in two independent experiments). Statistical significance compared with control samples (without TSA or romidepsin) is shown, based on the analyses in Figure S1C. *$p < 0.05$, ****$p < 0.0001$.

(C) Immunoblot confirming the depletion of individual class I HDACs 2 days post siRNA treatment. siNC: negative control siRNA.

(D) *DDB2*-deficient U2OS cells expressing EGFP-XPC were treated for 2 days with the indicated siRNAs. The accumulation of EGFP-XPC was monitored over time following local UVC stimulation and plotted as in (A and B). Two or three independent experiments were performed for each condition and the total number of cells analyzed (n =) is shown in gray. Statistical significance compared with siNC is shown based on the analysis in Figure S2A. **$p < 0.01$.

(E) *DDB2*-deficient U2OS cells expressing EGFP-XPC were irradiated with UVC (400 J/m^2) through isopore membrane filters. After 30 min incubation, immunofluorescence staining was carried out with the anti-H3K27ac antibody. Relative intensity of the H3K27ac stain in each irradiated area (identified by EGFP-XPC accumulation), in comparison with the entire nucleus, was calculated and plotted. Two independent experiments were performed, and the total number of cells analyzed (n =) is shown in gray. The mean with 95% confidence interval is shown for each sample. Statistical analysis was performed by one-way ANOVA followed by Tukey's HSD test. **$p < 0.01$.

(F) Either HDAC2 or HDAC3 fused to HaloTag 7 was ectopically expressed in *DDB2*-deficient U2OS cells expressing EGFP-XPC. After the cells were incubated for 30 min in the presence of the HaloTag TMR ligand, local UVC stimulation was applied to monitor the accumulation of HaloTag 7-fusion proteins. The TMR intensity in each stimulated area relative to the entire nucleus was calculated and plotted over time (the graph shows the means and SDs at each time point). Three independent experiments were performed and the total number of cells analyzed (n =) is shown in gray. Statistical analysis of endpoint data was performed by Student's *t* test (two tailed). ****$p < 0.0001$. See also Figure S6A.

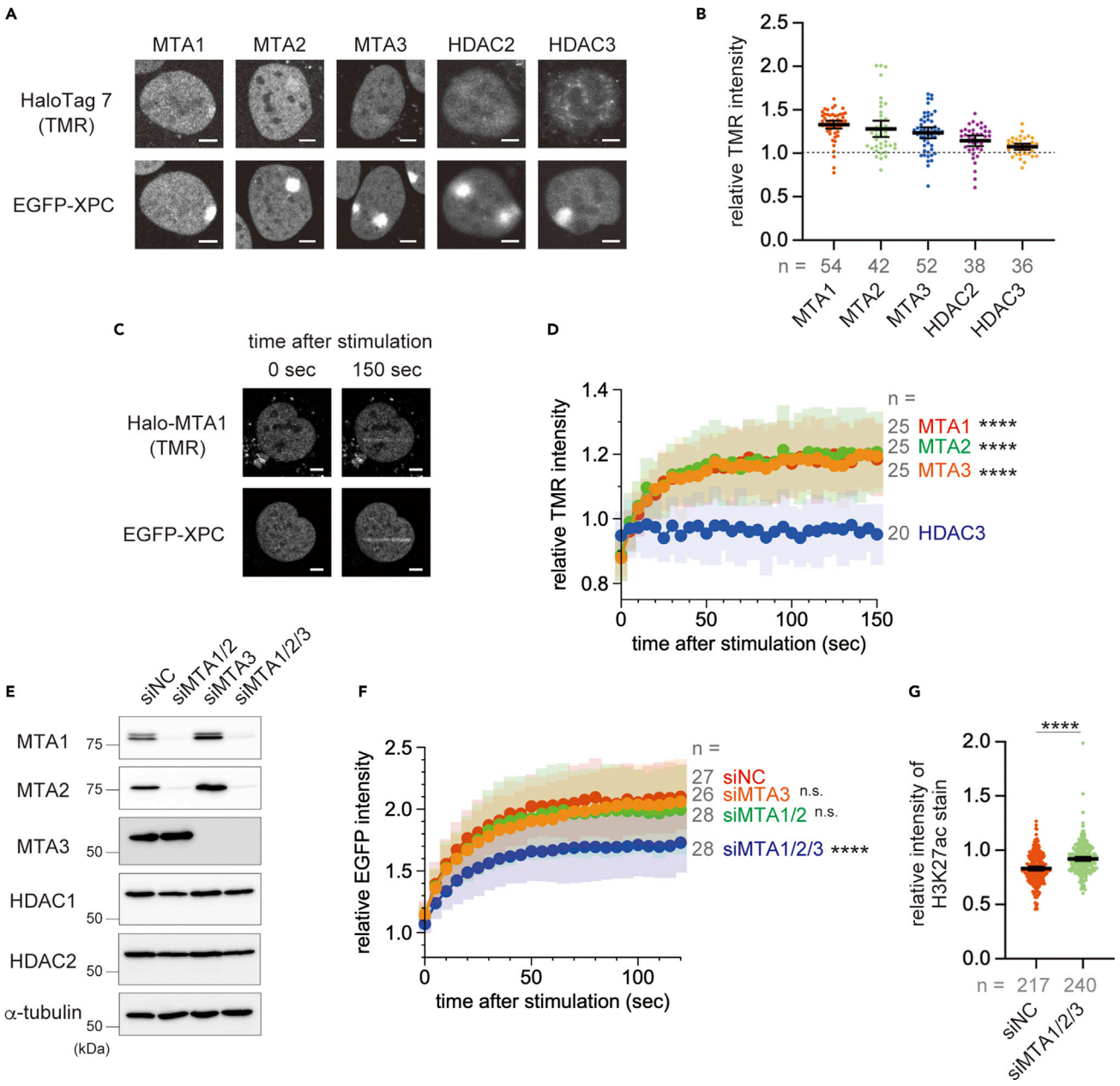

Figure 2. MTA proteins regulate histone deacetylation and XPC recruitment at LUD sites

(A) Three MTA proteins, HDAC2, and HDAC3 fused to HaloTag 7 were individually expressed in *DDB2*-deficient U2OS cells expressing EGFP-XPC. After labeling with the HaloTag TMR ligand, the cells were irradiated with UVC (400 J/m^2) through isopore membrane filters. After incubation for 15 min, the cells were fixed and observed under a confocal laser scanning microscope. Scale bar: 5 μm.

(B) Cells expressing the indicated proteins fused to HaloTag 7 were treated as shown in (A). Relative TMR intensity in each irradiated area (identified by EGFP-XPC accumulation), in comparison with the entire nucleus, was calculated and plotted. The mean with 95% confidence interval is shown for each sample. Two or three independent experiments were performed, and the total number of cells analyzed (n =) is shown in gray. One sample *t*-test (two tailed) was used to assess whether the mean value of each sample was greater than 1. p value: 3.9E-20 (MTA1), 2.9E-07 (MTA2), 4.6E-10 (MTA3), 2.6E-05 (HDAC2), 1.0E-04 (HDAC3).

(C) Laser-based local UVC stimulation was applied to cells co-expressing Halo-MTA1 and EGFP-XPC. Fluorescent images were acquired before and 150 s after stimulation. Scale bar: 5 μm.

(D) Indicated proteins fused to HaloTag 7 were ectopically expressed in *DDB2*-deficient U2OS cells expressing EGFP-XPC. After local UVC stimulation was applied as in (C), the accumulation of TMR fluorescence was monitored by time-lapse imaging. The TMR intensity in each stimulated area relative to the entire nucleus was calculated and plotted over time (the graph shows the means and SDs at each time point). Three independent experiments were

Figure 2. *Continued*

performed, and the total number of cells analyzed (n =) is shown in gray. Endpoint data were subjected to one-way ANOVA followed by Tukey's HSD test, and statistical significance compared with HDAC3 is shown. ****p < 0.0001. See also Figure S6A.

(E) Immunoblot confirming the depletion of individual MTA proteins 3 days post siRNA treatment.

(F) *DDB2*-deficient U2OS cells expressing EGFP-XPC were treated with the indicated siRNAs for 3 days. Upon local UVC stimulation, the accumulation of EGFP-XPC was monitored. The EGFP intensity in each stimulated area relative to the entire nucleus was calculated and plotted (the graph shows the means and SDs at each time point). Three independent experiments were performed, and the total number of cells analyzed (n =) is shown in gray. Statistical significance compared with siNC is shown, based on the analysis in Figure S6C. ****p < 0.0001.

(G) The three MTA proteins were simultaneously depleted in *DDB2*-deficient U2OS cells expressing EGFP-XPC. Local UVC irradiation (400 J/m^2) was performed through isopore membrane filters, and relative levels of H3K27ac in the irradiated areas were assessed as in Figure 1E. Two independent experiments were performed, and the total number of cells analyzed (n =) is shown in gray. Student's *t* test (two tailed) was used for statistical analyses. ****p < 0.0001.

wild-type HDAC2-Halo. Upon local UVC stimulation, we indeed observed an accumulation of HDAC2-Halo at LUD sites compared with HDAC3 (Figure 1F). Notably, immunofluorescence staining revealed that endogenous HDAC2 also localized at LUD sites (Figure S5A).

Next, we performed longer time course experiments to address how long the accumulation of HDAC2 and the hypoacetylation of histones persist at LUD sites. After laser-induced local DNA damage, the accumulation of HDAC2-Halo reached the maximal level around 10 min and then gradually decreased (Figures S5B and S5C). However, substantial accumulation was still discerned at 30 min post UVC stimulation. EGFP-XPC exhibited similar behavior, while the accumulation peaked earlier than that of HDAC2. This is not surprising because DNA lesions generated in non-acetylated chromatin regions can be recognized by XPC independently of HDACs. Reduction in H3K27ac was also analyzed at 10, 30, and 60 min after UVC irradiation through isopore membrane filters. Although the level of H3K27ac at LUD sites showed a tendency to decrease from 10 to 30 min post irradiation, statistical difference was not observed among these three time points (Figure S5D). These results suggest that HDAC2 associates with sites of DNA damage rather transiently, whereas reduction in H3K27ac is a more persistent phenomenon. Furthermore, we examined possible involvement of HDAC2 in the *DDB2*-dependent lesion recognition pathway. The accumulation of HDAC2-Halo was comparable between *DDB2*-proficient and -deficient U2OS cells (Figure S5E), whereas reduction in H3K27ac at LUD sites was slightly more pronounced in the presence of DDB2 (Figure S3C). These results raise the possibility that the *DDB2*-dependent lesion recognition pathway also involves histone deacetylation, which may be mediated by HDACs other than HDAC2.

The role of MTA proteins in histone deacetylation and recruitment of XPC

The catalytic functions of HDAC1/2 *in vivo* are activated by the assembly of higher-order complexes, such as NuRD, particularly through interactions with metastasis-associated family proteins (MTA1, 2, and 3) (Millard et al., 2013, 2014). We, therefore, wanted to examine the role that these proteins play in XPC recruitment. Each of the three MTA proteins was fused to HaloTag 7 (Halo-MTA1/2/3) and expressed in the *DDB2*-deficient U2OS cells. Upon local UVC irradiation through isopore membrane filters, all three MTA proteins significantly accumulated at the LUD sites (Figures 2A and 2B). The accumulation of HDAC2 was confirmed also with this method, while its enrichment at LUD sites seemed less pronounced than the MTA proteins. Comparable results were obtained following local laser-induced UVC stimulation (Figures 2C, 2D, and S6A). In these experiments, the accumulation of HDAC3 was only at a marginal or undetectable level (Figures 2B and S6A), excluding the possibility that these results were an artifact associated with HaloTag 7-fusion proteins. Notably, the accumulation of MTA2 to LUD sites did not depend on either DDB2 or XPC (Figure S6B). Next, the expression of the endogenous MTA proteins was suppressed by siRNAs (Figure 2E). Recruitment of EGFP-XPC upon local UVC stimulation was significantly compromised when all three MTA proteins were depleted simultaneously (Figures 2F and S6C), while EGFP-XPC mobility was increased (Figures S6D and S6E). Furthermore, the suppression of H3K27ac at LUD sites was also alleviated by simultaneous depletion of all three MTA proteins (Figure 2G). These results indicate that the MTA proteins have redundant functions in the recruitment of XPC, presumably through the complex assembly and activation of HDACs at sites of DNA damage.

The acetylation state of histones regulates XPC chromatin localization

Given that HDACs are activated at DNA damage sites and facilitate the recruitment of XPC, it was crucial to ask whether the acetylation state of the histone proteins affects subnuclear localization of XPC. To address this question, we next examined XPC localization in mouse cells. It has been shown that pericentromeric

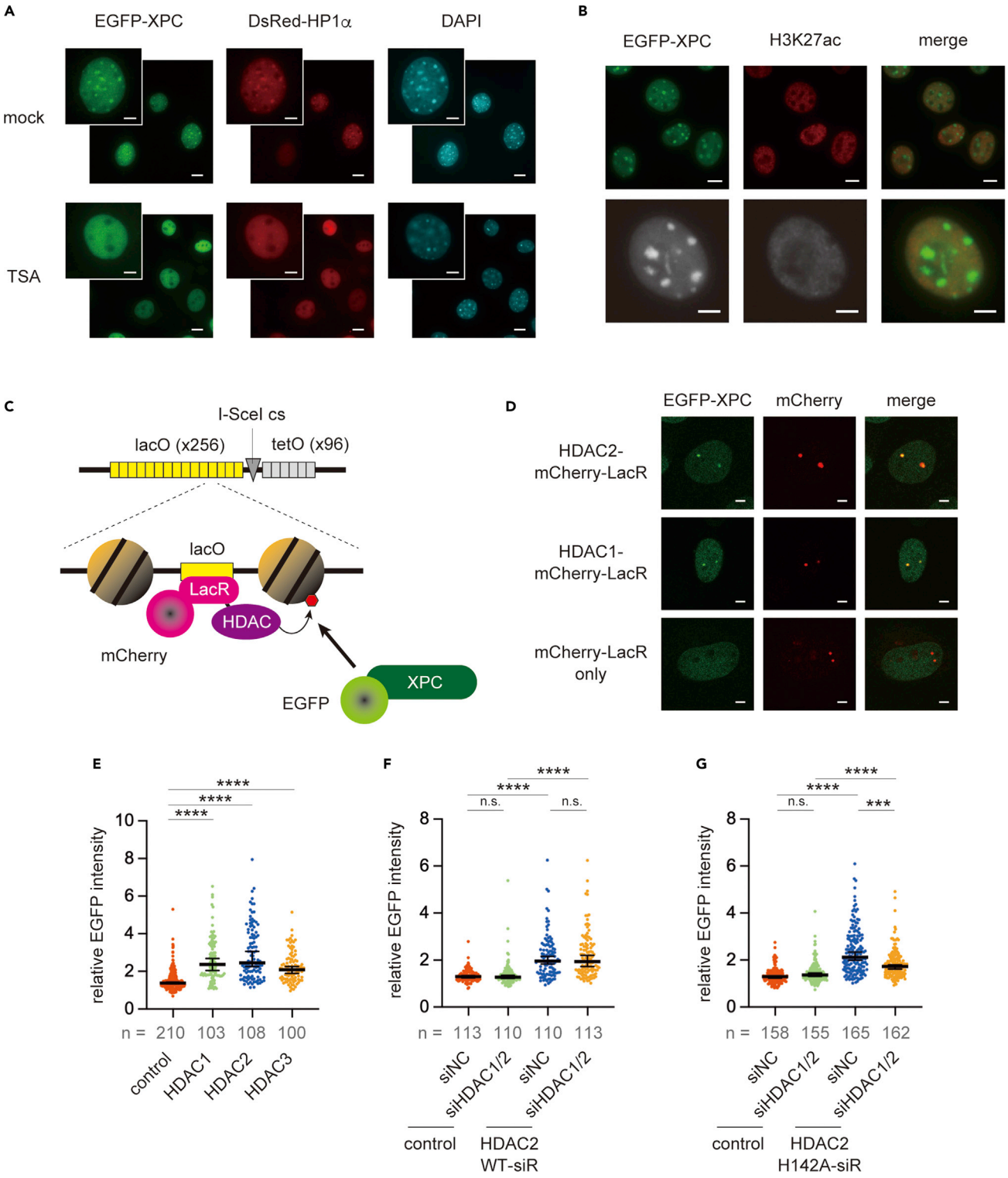

Figure 3. XPC localizes to hypoacetylated chromatin regions

(A) EGFP-XPC and DsRed-HP1α were simultaneously expressed in *Xpc*-deficient MEFs. The cells were treated for 6 h with 0 or 2 μM TSA, fixed, counterstained with DAPI, and observed under a fluorescence microscope. Scale bar: 10 μm (wide-field image), 5 μm (enlarged image).

(B) *Xpc*-deficient MEFs expressing EGFP-XPC were fixed and stained with anti-H3K27ac antibody. Scale bar: 10 μm (upper panel), 5 μm (lower panel).

(C) Schematic illustration of the LacO-LacR tethering system.

Figure 3. *Continued*

(D) Cells harboring *lacO* arrays and stably expressing EGFP-XPC were transfected with constructs for the expression of HDAC2-mCherry-LacR, HDAC1-mCherry-LacR, or mCherry-LacR alone, and incubated for 2 days. After pre-extraction and fixation, the cells were observed under a confocal laser scanning fluorescence microscope. Representative images of transfected cells are shown. Scale bar: 5 μm.

(E) Relative EGFP intensity at the *lacO* arrays (marked by mCherry fluorescence) in comparison with the entire nucleus was calculated and plotted using fluorescent images from (D). HDAC3-mCherry-LacR was also included in this quantitative analysis. Two independent experiments were performed, and the total number of cells analyzed (n =) is shown in gray. The median with 95% confidence interval is shown for each sample. Statistical difference from control (mCherry-LacR only) was assessed by Kruskal-Wallis test followed by Dunnett's test. ****$p < 0.0001$.

(F and G) Cells stably expressing EGFP-XPC were treated with siNC or a mixture of siRNAs targeting HDAC1 and HDAC2 (siHDAC1/2). Subsequently, mCherry-LacR fused to siRNA-resistant (siR) wild-type (D) or H142A mutant HDAC2 (E) was transiently expressed. mCherry-LacR alone was used as a control. Relative EGFP intensity at the *lacO* arrays in comparison with the entire nucleus was calculated and plotted as in (E). Two independent experiments were performed, and the total number of cells analyzed (n =) for each condition is shown in gray. Statistical analysis was performed by Kruskal-Wallis test followed by Dunnett's test. ***$p < 0.001$, ****$p < 0.0001$.

chromatin in mouse cells often exhibits a characteristic punctate distribution within the nucleus, called "chromocenters" (Guenatri et al., 2004), which corresponds to heterochromatin characterized by histone hypoacetylation and heterochromatin protein 1 (HP1) association through its interaction with H3K9me3. When EGFP-tagged human XPC was stably expressed in *Xpc*-deficient mouse embryonic fibroblasts (MEFs), we found that a substantial fraction of EGFP-XPC localized to chromocenters (Figures 3A and S7A). It should be noted that this localization was observed in cells without exposure to exogenous DNA-damaging agents. Mutant XPC harboring a pathogenic amino acid substitution (Trp690Ser) still exhibited a punctate distribution, indicating that the DNA-binding activity of XPC is not essential for its association with the chromocenters (Figure S7B) (Chavanne et al., 2000; Yasuda et al., 2007). Notably XPC, like HP1α, was dispersed from chromocenters upon treatment with the HDAC inhibitor, TSA (Figures 3A and S7A), while depletion of Suv39h1/2, the histone methyltransferases responsible for H3K9me3, resulted in HP1α dispersal but had little effect on XPC localization (Figures S7C and S7D). These data suggest that distinct mechanisms underlie the chromocenter localization of XPC and HP1α. Because XPC and acetylated histones tended to show mutually exclusive localization (Figure 3B), hypoacetylated chromatin appeared to be more relevant in the regulation of subnuclear XPC localization.

To further address the hypothesis that histone deacetylation regulates the XPC localization, we took advantage of the U2OS-LacO-I-SceI-TetO cells, which harbor 256 copies of the *lac* operator (*lacO*) sequence at two specific genomic loci (Figure 3C) (Burgess et al., 2014). First, a stable transformant expressing EGFP-XPC was isolated with this cell line. We found that EGFP-XPC localized at the *lacO* arrays when HDAC2- or HDAC1-mCherry-LacR, but not mCherry-LacR alone, was expressed in these cells (Figures 3D and 3E). Immunofluorescence staining confirmed a reduction in histone acetylation around the *lacO* arrays bound by HDAC2 (Figures S8A and S8B). Notably, tethering of HDAC3 also induced histone deacetylation and XPC recruitment at the *lacO* arrays (Figures 3E, S8A, and S8B), suggesting that the major determinant of XPC re-localization is histone deacetylation, rather than the specific protein-protein interaction between XPC and HDAC2 (or its associating factors).

To examine whether this re-localization of XPC depends on HDAC catalytic activity, HDAC2 H142A mutant was examined. Like the rescue experiment of EGFP-XPC accumulation (Figures S4E and S4F), we took advantage of simultaneous HDAC1/2 depletion and siRNA-resistant HDAC2 (Figure S8C), because tethering of HDAC2^{H142A} remained proficient not only in the recruitment of EGFP-XPC but also in histone deacetylation at the *lacO* arrays. As expected, simultaneous depletion of endogenous HDAC1/2 compromised the recruitment of EGFP-XPC by HDAC2^{H142A}, but not wild-type HDAC2 (Figures 3F and 3G). Furthermore, we confirmed that XPC recruitment induced by tethered HDAC2 was unaffected by the depletion of endogenous DDB2 (Figure S8D). Taken together, we conclude that subnuclear localization of XPC can be regulated by the acetylation state of histones, even in the absence of DNA damage.

The disordered middle region of XPC mediates the interaction with histone H3

We next examined which region of the XPC protein is responsible for the regulation of its localization. Several XPC deletion mutants fused to EGFP were constructed and stably expressed in the *Xpc*-deficient MEFs (Figures 4A and 4B), revealing that the region encompassing amino acids 325 through 512 was necessary and sufficient for chromocenter localization (Figures 4C and 4D). This intrinsically disordered middle (M) region, which divides the transglutaminase-homology domain (TGD) into two parts (Figure 4A) (Anantharaman, 2001; Bunick et al., 2006; Kakumu et al., 2017), is poorly conserved and absent from the

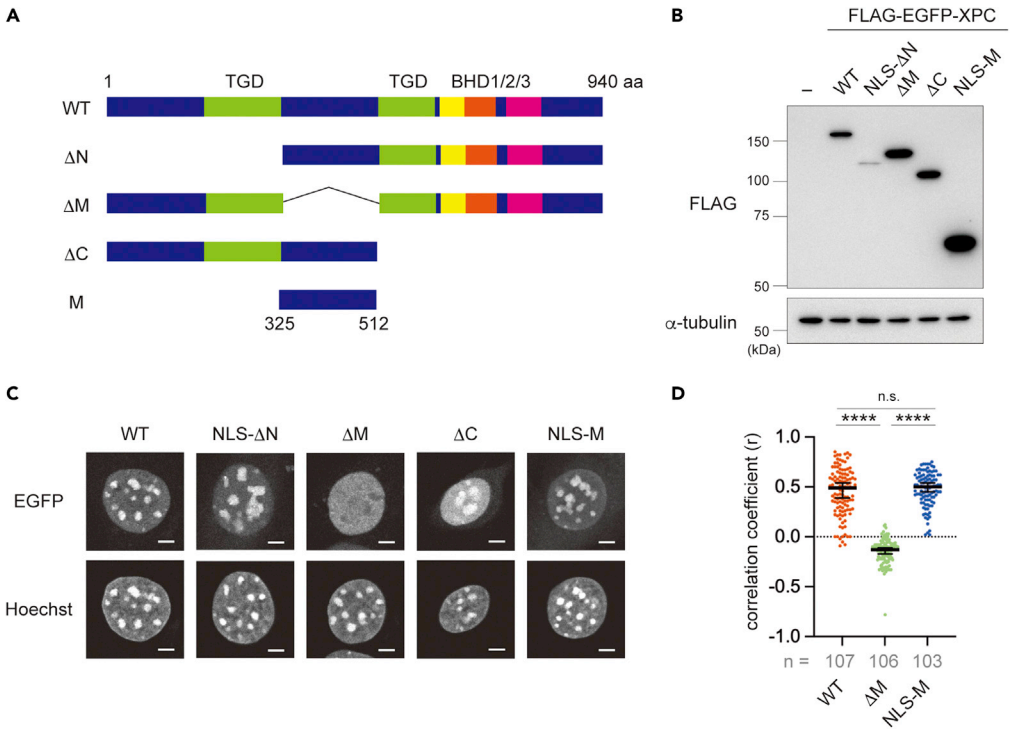

Figure 4. The XPC-M region regulates the subnuclear localization of XPC

(A) Deletion mutants of human XPC used in this study. Positions of the transglutaminase-homology domain (TGD) and three β-hairpin domains (BHD1/2/3) are indicated.

(B) The wild-type and mutant XPC proteins in (A) were fused to the FLAG-EGFP tandem tag and stably expressed in *Xpc*-deficient MEFs. Immunoblot confirming the protein expression is shown.

(C) The cells used in (B) were fixed, counterstained with Hoechst 33342, and observed under a confocal laser scanning fluorescence microscope. Scale bar: 5 μm.

(D) Correlation coefficients between EGFP and Hoechst 33342 signals were calculated and plotted for individual nuclei using images from (C). Two independent experiments were performed, and the total number of cells analyzed (n =) is shown in gray. The median with 95% confidence interval is shown for each sample. Statistical analysis was carried out by Kruskal-Wallis test followed by Dunnett's test, and only the results among WT, ΔM, and NLS-M are shown. ****$p < 0.0001$.

budding yeast XPC homolog, RAD4. We prepared recombinant XPC protein lacking the M region ($XPC^{\Delta M}$), which retained the ability to form a complex with RAD23B (Figure 5A) and exhibited activity in cell-free NER dual incision assays comparable to wild-type XPC (XPC^{WT}) (Figure 5B). Therefore, we concluded that the M region is dispensable for the basal NER function of XPC *in vitro*.

We have previously reported direct physical interactions between XPC and histone H3 (Kakumu et al., 2017). Therefore, we postulated that the XPC-M region may be involved in the interaction with histone H3 in an acetylation-regulated manner. Because the N-terminal tail of histone H3 appears to be important for the interaction with XPC (Kakumu et al., 2017), N-terminal sequences encompassing amino acids 1–20 or 1–41 fused to glutathione *S*-transferase (GST) were purified for use in pull-down experiments (Figure 5C). As expected, the XPC^{WT}-RAD23B heterodimer exhibited specific binding to the H3 N-terminal tail sequences, an interaction that was weakened by deletion of XPC-M (Figures 5D and 5E). Next, the XPC-M region alone fused to the FLAG tag was purified (Figure 5A), which interacted with the N-terminal tail sequences efficiently (Figures 5F and 5G). Notably, these interactions were severely compromised by acetylation-mimetic Lys-to-Gln substitutions in the H3 N-terminal. Similar results were obtained when another pull-down system using biotinylated synthetic peptides (1–21) was used. The XPC-M region efficiently bound to the histone peptides, which was abrogated by the pre-treatment of the peptides with the purified recombinant histone acetyltransferase CBP (Figure 5H). It was confirmed by LC/MS/MS analyses that ~90% of the peptides acquired at least one acetyl group after the reaction containing CBP and acetyl-CoA (Figure S9). These results strongly suggest that the interaction between the XPC-M region and the N-terminal tail of histone H3 regulates XPC localization to hypoacetylated chromatin.

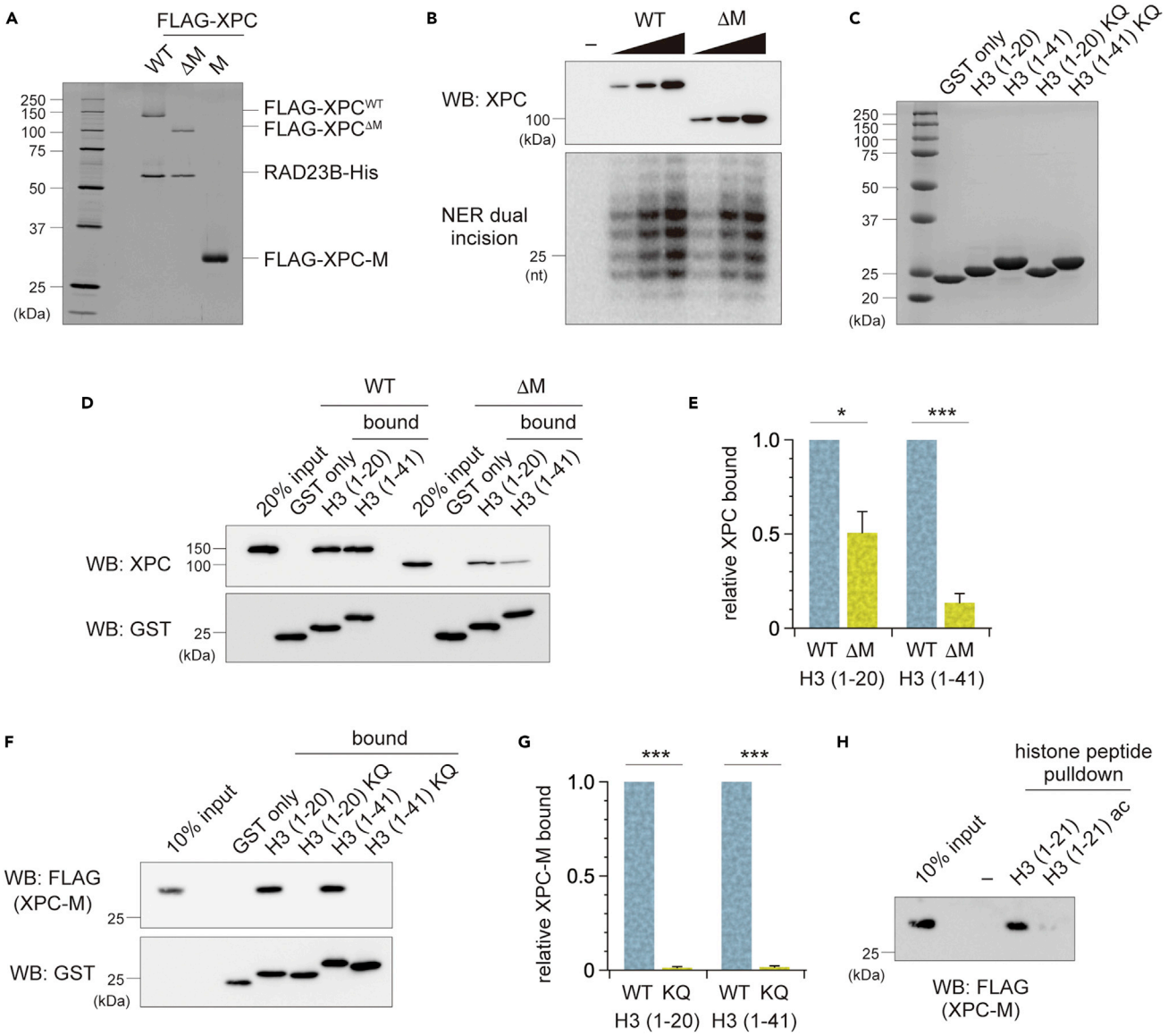

Figure 5. The XPC-M region interacts with the deacetylated N-terminal tail of histone H3

(A) Purified recombinant XPC-RAD23B heterodimer (WT or ΔM) and XPC-M were subjected to SDS-PAGE followed by silver staining.

(B) Cell-free NER dual incision assays were performed with increasing concentration of purified XPC-RAD23B complex. (upper panel) Immunoblot to confirm comparable amounts of wild-type and mutant XPC were included in the assay. (lower panel) Dual incision products generated in the corresponding reactions.

(C) Purified GST and GST fusion proteins harboring N-terminal tail sequences (wild type or KQ mutant) of histone H3 were subjected to SDS-PAGE, followed by Coomassie Blue staining.

(D and E) GST pull-down assays using XPC-RAD23B complex with or without the XPC-M region. Bound XPC was quantified from the images in (D), and normalized to the level of bound XPC^{WT} (E). The graph in (E) shows the mean and SEMs from three independent experiments. Statistical significance of the differences was assessed by Student's *t* test (two tailed). *$p < 0.05$, ***$p < 0.001$.

(F and G) GST pull-down assays with XPC-M. Quantifications were performed as in (D and E), and the mean and SEMs were calculated from three independent experiments. ***$p < 0.001$.

(H) Biotinylated synthetic peptides corresponding to the N-terminal 21 amino acids of histone H3 were pre-treated with the recombinant histone acetyltransferase CBP in the presence or absence of acetyl-CoA, and were used to pull down XPC-M.

The XPC-M region regulates GG-NER

To address whether the M region affects the GG-NER, EGFP-tagged XPC^{WT} and $XPC^{\Delta M}$ were stably expressed in U2OS cells in which both the endogenous *XPC* and *DDB2* genes were disrupted ($U2OS^{DKO}$) (Figure 6A). Upon local UVC stimulation, the accumulation of $XPC^{\Delta M}$ at LUD sites was compromised

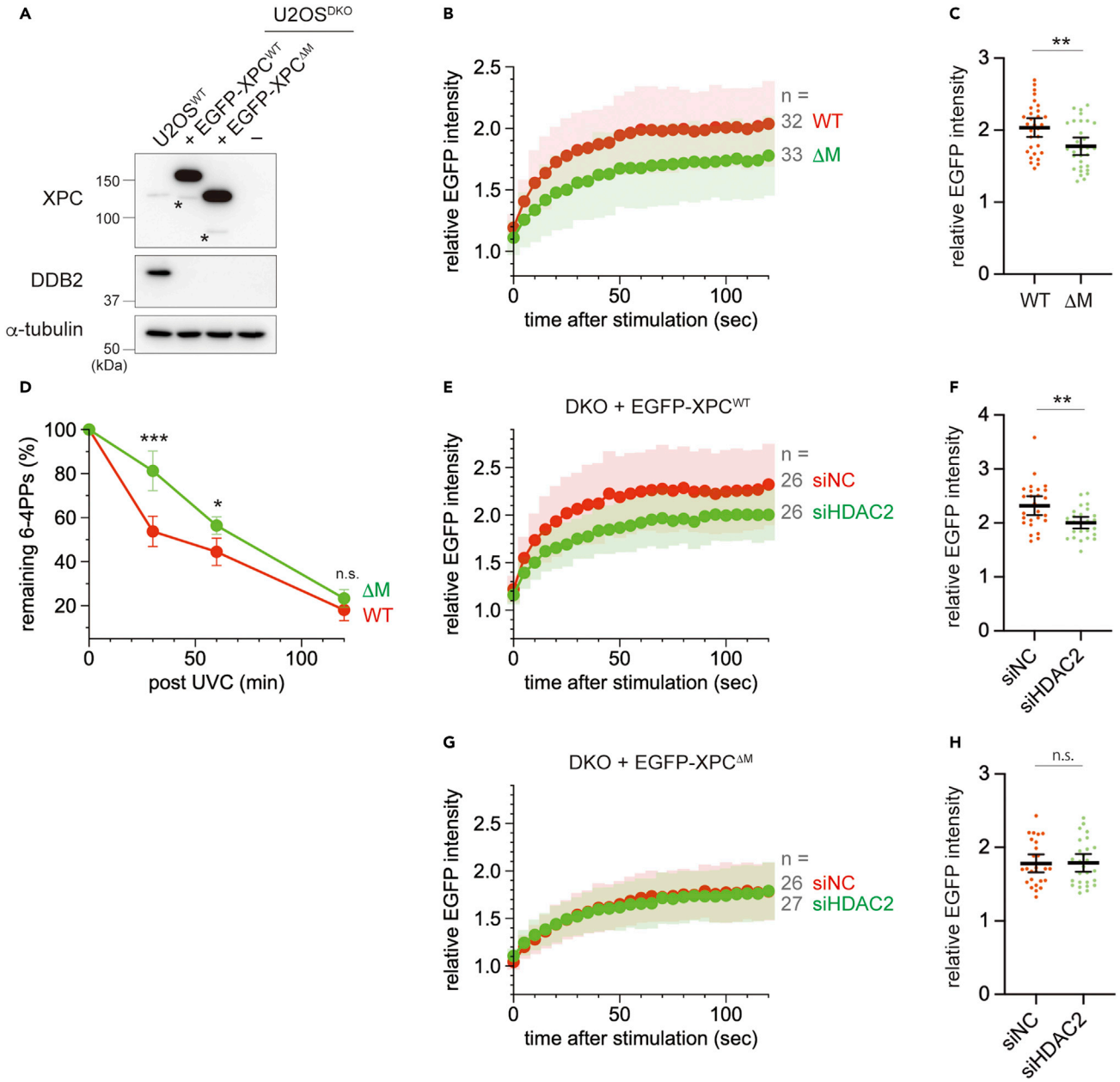

Figure 6. XPC-M enhances GG-NER *in vivo*

(A) Immunoblot analysis confirming the absence of endogenous XPC and DDB2 in the U2OS^{DKO} cells and the expression of EGFP-XPC (WT or ΔM). The bands indicated by asterisk represent truncated or degraded protein products of EGFP-XPC.

(B) Local UVC stimulation was applied to U2OS^{DKO} cells expressing EGFP-XPC (WT or ΔM), and the accumulation of EGFP fluorescence at LUD sites was monitored by time-lapse imaging. The EGFP intensity in each stimulated area relative to the entire nucleus was calculated and plotted (the graph shows the means and SDs at each time point). Three independent experiments were performed, and the total number of cells analyzed (n =) is shown in gray.

(C) Endpoint data (at 120 s post stimulation) from (B) were plotted. The mean with 95% confidence interval is shown for each sample. Statistical significance of the difference was assessed by Student's *t* test (two tailed). **$p < 0.01$.

(D) U2OS^{DKO} cells expressing EGFP-XPC (WT or ΔM) were globally exposed to UVC (10 J/m^2) and incubated for various times. The amount of residual 6-4PP was quantified based on immunofluorescence staining as shown in Figure S11. The mean and SEMs were calculated from four independent experiments. Student's *t* test was used to assess statistical difference at each time point. *$p < 0.05$, ***$p < 0.001$.

(E) U2OS^{DKO} cells expressing EGFP-XPC^{WT} were pre-treated for 2 days with either siHDAC2 or siNC. Upon local UVC stimulation, the accumulation of EGFP fluorescence at LUD sites was monitored. Relative EGFP intensity in each stimulated area in comparison with the entire nucleus was calculated and plotted over time (the graph shows the means and SDs at each time point). Three independent experiments were performed, and the total number of cells analyzed (n =) is shown in gray.

Figure 6. *Continued*

(F) Endpoint data extracted from (E) were plotted. The mean with 95% confidence interval is shown for each sample. Statistical difference was assessed by Student's *t* test (two tailed). **$p < 0.01$.

(G and H) U2OS^{DKO} cells expressing EGFP-XPC$^{\Delta M}$ were analyzed as in (E and F). Three independent experiments were performed, and the total number of cells analyzed (n =) is shown in gray.

compared with XPC^{WT} (Figures 6B and 6C), although FRAP analyses revealed that XPC$^{\Delta M}$ exhibited greater mobility in the nucleus (Figures S10A and S10B).

Next, repair kinetics of UV-induced DNA photolesions in these cell lines was compared. For this purpose, we set up a new imaging-based assay, in which immunofluorescence intensities with the anti-6-4PP antibody were quantified for individual cell nuclei (Figure S11A). When cells treated with various doses of UVC were immediately fixed and subjected to immunofluorescence staining, each sample showed a linear correlation between the levels of 6-4PPs and DNA content (Figure S11B), and calculated medians of the 6-4PP level normalized by DNA content were linearly in proportion to the UV doses (Figures S11C and S11D). This method could be applied to cells that were incubated for various periods of time after UV irradiation, which allowed assessment of repair kinetics in a reasonable manner (Figures S11A, S11C, and S11E). With this assay, XPC$^{\Delta M}$-expressing cells showed significantly slower removal of 6-4PPs from genomic DNA, particularly at early time points, than XPC^{WT} cells following global UVC irradiation (Figure 6D).

Finally, we examined the effect of HDAC2 depletion on GG-NER (Figure S10C). Local UVC stimulation revealed that recruitment of XPC^{WT} was compromised by the depletion of HDAC2 (Figures 6E and 6F), as observed with the *DDB2* single knockout background (Figure 1D). By striking contrast, the accumulation of XPC$^{\Delta M}$ was unaffected by the presence or absence of HDAC2 (Figures 6G and 6H). Taken together, these results indicate that the XPC-M region plays a stimulatory role in GG-NER in conjunction with the deacetylation of histones.

DISCUSSION

A role for HDACs in DNA lesion recognition during GG-NER

We previously showed that HDAC inhibitors, such as TSA and sodium butyrate (NaBu), compromise the recruitment of XPC to sites of DNA damage and the removal of UV-induced 6-4PPs (Kakumu et al., 2017). Mammalian cells express 18 HDAC species (HDAC1-11 and SIRT1-7), which are divided into five classes (class I, IIa, IIb, III, and IV) based on amino acid sequence similarities. TSA inhibits all but class III (Sirtuin family) HDACs, while NaBu targets class I and IIa specifically (Milazzo et al., 2020). In the present study, the accumulation of XPC at LUD sites was significantly diminished following treatment with the class I-specific inhibitor, romidepsin (Figure 1B). Based on analyses of individual class I HDACs, we concluded that HDAC1 and HDAC2 have redundant functions during XPC recruitment. These results were obtained from *DDB2*-deficient U2OS cells, indicating that HDAC1/2 are involved in UV-DDB-independent lesion recognition.

The role of histone acetylation in NER is somewhat controversial. Overexpression of HDACs has been reported in some melanoma cells (Krumm et al., 2016; Liu et al., 2016), while treatment of these melanoma cells with NaBu compromised the removal of psoralen-induced DNA adducts by NER (Toyooka and Ibuki, 2009). However, HDAC inhibition with NaBu has been shown to enhance NER in UV-irradiated normal human fibroblasts (Smerdon et al., 1982). The expression of DDB2 depends on p53 status (Hwang et al., 1999; Tan and Chu, 2002), which could explain the difference between normal human fibroblasts and melanoma cells. In addition, considering the DNA-binding specificity of UV-DDB (Payne and Chu, 1994; Scrima et al., 2008; Tang and Chu, 2002), bulky lesions induced by chemical compounds, such as psoralen, are processed likely via the UV-DDB-independent pathway. We believe that the role of HDACs may differ in the UV-DDB-dependent and -independent lesion recognition pathways, and the observed effects of HDAC inhibitors on GG-NER could vary depending on the type of DNA lesions and cell type. Recently, it has been reported that deacetylation of histone H3K14 by HDAC3 facilitates the recruitment of XPC to LUD sites (Nishimoto et al., 2020). Because the removal of UV-induced CPDs was affected by depletion of HDAC3, this mechanism appears to concern the UV-DDB-dependent pathway. Although our results indicate that the contribution of HDACs other than HDAC1/2 is marginal in the absence of UV-DDB, it is notable that H3K27ac reduction at LUD sites seems slightly more pronounced in *DDB2*-proficient cells (Figure S3C).

This suggests the possibility that UV-DDB may recruit certain HDAC species to induce histone deacetylation at DNA damage sites, which could contribute to the promotion of XPC recruitment. However, it is unlikely that such a small difference in H3K27ac fully accounts for the robust stimulation of XPC recruitment by UV-DDB, as reorted previously (Kusakabe et al., 2019). We think that the DDB2-dependent recruitment of XPC must include multiple factors, such as the physical interaction between XPC and UV-DDB (Sugasawa et al., 2005), the ubiquitin-proteasome system (Puumalainen et al., 2014), and other post-translational protein modifications, such as poly(ADP-ribosyl)ation (Pines et al., 2012) and methylation (Pogliano et al., 2017).

UV-DDB bound at UV-induced photolesions acts as a landmark targeted by XPC. It is conceivable that global decondensation of chromatin following HDAC inhibition is advantageous for XPC to locate sites bound by a large protein complex, such as UV-DDB. By contrast, the UV-DDB-independent lesion recognition pathway requires the discrimination of far more subtle differences in DNA structure by XPC. Single-molecule analyses have revealed that XPC first associates with undamaged DNA and searches for sites of damage by diffusion along DNA fibers (Cheon et al., 2019; Kong et al., 2016). Although global chromatin opening by hyperacetylation of histones increases accessibility to lesions, it also enhances non-specific interactions of XPC with intact chromatin, which consequently could reduce the overall efficiency of lesion recognition.

Recruitment of HDACs to DNA lesions

The data presented here suggest that HDAC1/2 plays a pivotal role in the deacetylation of histones around UV-induced DNA photolesions. Upon local UVC stimulation, we observed an accumulation of HDAC2 and MTA proteins (Figures 1F, 2A, 2B, 2C, and 2D), which have been shown to interact with and activate HDAC1/2 (Millard et al., 2013, 2014), at LUD sites. The depletion of HDAC2, or the simultaneous depletion of all three MTA proteins, significantly attenuated XPC accumulation and UVC-irradiation-dependent histone deacetylation (Figures 1D, 1E, 2E, 2F, and 2G). These results indicate that HDAC1/2 and MTAs cooperate at DNA damage sites to deacetylate local histones and facilitate XPC recruitment.

Notably, HDAC1/2 and the MTA proteins are components of the NuRD complex, which possesses both histone deacetylase and ATP-dependent chromatin remodeling activities (Xue et al., 1998; Zhang et al., 1999). The NuRD complex contains two HDAC molecules, either HDAC1 or HDAC2, in any combination. These two HDAC species are closely related and have redundant functions. Although depletion of HDAC1 alone did not affect the recruitment of XPC or the deacetylation of histones at LUD sites in our experiments (Figures 1D and 1E), this is very likely because HDAC1 protein is less abundant than HDAC2 in U2OS cells (Figure S4A) (Geiger et al., 2012). Nevertheless, our results raise the fascinating possibility that the NuRD complex is recruited to, or assembled at, DNA damage sites and is involved in the initiation of GG-NER. The DDB2/XPC-independent accumulation of MTAs to LUD sites (Figure S6B) also suggests the presence of such HDAC complexes prior to the recruitment of XPC. In addition to HDACs (HDAC1/2) and MTA proteins (MTA1/2/3), the NuRD complex contains ATPases (CHD3/4), methyl-cytosine DNA-binding domain proteins (MBD2/3), and GATA-type zinc finger proteins (GATAD2A/B) in a number of different combinations, contributing to possible functional diversity. A subset of NuRD complexes with specific subunit compositions could be relevant for UV-DDB-independent lesion recognition during GG-NER. Alternatively, it is possible that HDAC1/2 and the MTA proteins are assembled into a novel complex devoted to GG-NER regulation. The identification of this precise complex composition is crucial to understand the mechanisms underlying HDAC activation at DNA damage sites and is a subject for future study.

The regulation of XPC localization and implications for DNA damage recognition

Here, we show that subnuclear localization of XPC is regulated by histone modifications, especially acetylation, in a DNA damage-independent manner. First, XPC in MEFs tends to localize preferentially in chromocenters, which form heterochromatin characterized by the presence of H3K9me3 and HP1 binding (Figure 3A). This localization is not through the non-specific binding of XPC to condensed DNA regions, as XPC W690S mutant protein is still able to localize at chromocenters (Figure S7B). However, XPC localization to chromocenters is abrogated by the inhibition of HDACs (Figures 3A and S7A) and unaffected by the loss of H3K9me3 (Figure S7D). These data indicate that a major determinant of XPC localization is the presence of hypoacetylated histones, rather than highly condensed heterochromatin. This is further supported by our data from LacO-LacR tethering experiments, which showed that the

tethering of HDAC1/2 on *lacO* arrays induced local deacetylation of histone proteins and the recruitment of XPC, without exogenous DNA damage (Figures 4 and S8). On the other hand, it is not excluded that HDAC1/2 also target unidentified non-histone proteins in chromatin, acetylation of which negatively regulate DNA damage recognition by XPC in conjunction with histones.

In an attempt to understand the mechanism underlying such XPC localization, we identified a novel role for the structurally disordered XPC-M region, for which no function has been assigned (Bunick et al., 2006). $XPC^{\Delta M}$ mutant protein interacted with RAD23, and its activity in cell-free NER assays was indistinguishable from that of XPC^{WT} (Figures 5A and 5B), indicating that the M region is dispensable for its basal NER function. However, when $XPC^{\Delta M}$ was expressed in *XPC*-deficient cells, global UV-DDB-independent removal of 6-4PPs was significantly compromised in comparison with XPC^{WT}-expressing control cells (Figure 6D). Intriguingly, the XPC-M region was necessary and sufficient for localization to hypoacetylated chromatin *in vivo* (Figures 3D and 3E), and for interactions with non-acetylated histone H3 tails *in vitro* (Figures 5D–5H). Together, these data suggest that DNA lesions induce alterations in the neighboring chromatin structure, including the deacetylation of histones, which attract XPC via an interaction between the M region and the histone tails (Figure 7). This may contribute to the increased local concentration of XPC and, consequently, the probability that XPC will encounter a DNA lesion. It should be noted that the distribution of histone modifications is not uniform throughout the genome, so that deacetylation may not be necessary for all lesion recognition events by XPC. For instance, because XPC appears to localize preferentially in hypoacetylated chromatin (such as heterochromatin), it is conceivable that DNA lesions generated in such chromatin regions are recognized and repaired without the need for HDAC recruitment. This could explain why the accumulation of HDAC2 at LUD sites appeared to peak later than that of XPC (Figures S5B and S5C). In budding yeast, the XPC homolog RAD4 does not have the M region and the TGD exists as a continuous domain. This lack of an M region could be related to the relatively small size of the yeast genome and/or simple and open organization of yeast chromatin. Furthermore, there are mechanistic differences in the recognition of lesions during GG-NER between yeast and mammals. For example, GG-NER in budding yeast requires the RAD7-RAD16 complex instead of UV-DDB (Miller et al., 1982; Verhage et al., 1994). RAD7 reportedly interacts with SIR3, a component of the gene silencing complex in yeast, and this interaction may allow damage recognition by RAD4 in transcriptionally inactive chromatin (Paetkau et al., 1994).

While deacetylated histones are associated with compacted chromatin and transcriptional repression, it remains to be addressed whether such chromatin condensation is involved in lesion recognition by XPC. Considering that the original chromatin structure must be retained after the completion of repair, it seems unlikely that extensive condensation is established. If histone deacetylation precedes the lesion recognition by XPC, the chromatin restoration must involve re-acetylation thereafter. It is currently unclear when such acetylation occurs, and it is conceivable that the re-acetylation of histones may facilitate the release of XPC and progress of the following repair process. However, we think that this is unlikely, because such a mechanism would not be relevant to GG-NER in non-acetylated chromatin. While our results consistently point to negative roles for histone acetylation, it is possible that DNA lesion recognition by XPC is positively regulated by other histone modifications. Because lysines are targeted for many different post-translational modifications, deacetylation may be required to allow for the transient conversion of histone modifications. On the other hand, it has been reported that a sub-population of XPC localizes to the promoter regions of actively transcribed genes (Cattoglio et al., 2015; May et al., 2010). Given the proposed roles for XPC in transcriptional regulation, different mechanisms could control XPC localization to promoter regions; for instance, through interactions with transcription factors, such as TFIIH and SOX2/OCT4.

In conclusion, our present study unveiled a novel molecular mechanism for the recognition of DNA lesions by XPC in the absence of UV-DDB. The generation of DNA damage induces the recruitment or assembly of functional HDAC complexes and the deacetylation of local histones, which attracts XPC through an interaction with the XPC-M region. The presence of chromatin remodelling complexes, such as NuRD, may be relevant for subsequent GG-NER steps, since biochemical studies have revealed that DNA lesion sites within nucleosome cores are prevented from recognition by XPC (Hara et al., 2000; Ura et al., 2001; Yasuda et al., 2005), but not by UV-DDB (Matsumoto et al., 2019; Osakabe et al., 2015). UV-DDB *in vivo* appears to exist on internucleosomal DNA preferentially (Fei et al., 2011), suggesting that it induces alteration of chromatin structures, such that the lesion sites become accessible to XPC. Notably, it has been reported that the histone methyltransferase ASH1L is recruited to chromatin by UV-DDB, which

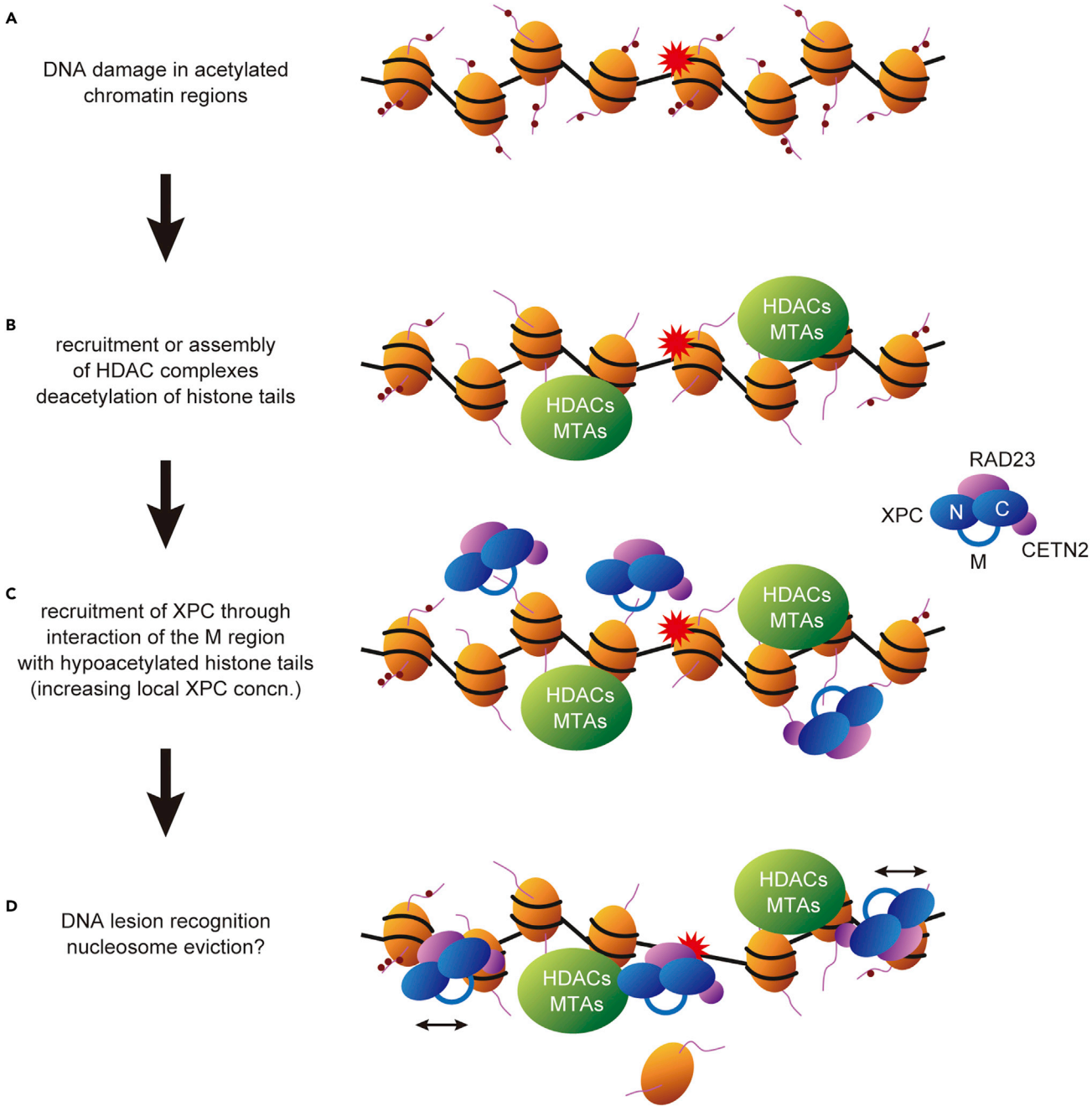

Figure 7. A model for the role of HDACs in the promotion of DNA lesion recognition by XPC

(A–D) Upon induction of DNA damage in acetylated chromatin regions (A), protein complexes containing HDAC1/2 and MTAs are recruited or assembled, leading to deacetylation of histone tails around the site of the lesion (B). XPC is recruited through the interaction between the disordered XPC-M region and non-acetylated histone tails, resulting in an elevated local XPC concentration (C). Given that XPC tends to pre-localize in hypoacetylated chromatin regions, (B) is essential if DNA damage occurs in an acetylated histone-rich region. XPC searches for a DNA lesion by diffusion along chromatin fibers, and the removal of the histone octamer from the site of the lesion is a prerequisite for an interaction with XPC (D), to which the chromatin remodeling function of HDAC complexes (such as NuRD) could be relevant.

then promotes CPD repair presumably through interaction of XPC with H3K4me3-containing nucleosomes (Pogliano et al., 2017). It is possible that the DDB2-independent lesion recognition pathway also involves the methylation or other modifications of lysine residues in histones, to which deacetylation occurs as a pre-requisite particularly in acetylated chromatin regions. Furthermore, PARP1 has been shown to interact with

XPC and facilitate DNA lesion recognition in a DDB2-independent manner (Robu et al., 2017). Although precise targets of the poly(ADP-ribosyl)ation remain to be identified, this also could play a role in regulation of the XPC-histone interactions. Further studies are necessary to shed light on the precise mechanism for the efficient removal of "difficult to detect" DNA lesions.

Limitations of the study

The role for HDACs uncovered in this study is relevant to the removal of DNA lesions that are generated in acetylated chromatin regions. Therefore, the impacts of HDAC- or MTA-depletion on the overall efficiency of GG-NER would be less pronounced, if compared with the loss of XPC-M region (Figure 6D), which could affect lesion recognition globally through the interaction with histone H3 tail. It remains to be addressed whether the genome-wide localization of XPC and histone modifications determines the priority and efficiency of DNA lesion removal.

STAR★METHODS

Detailed methods are provided in the online version of this paper and include the following:

- KEY RESOURCES TABLE
- RESOURCE AVAILABILITY
  - Lead contact
  - Materials availability
  - Data and code availability
- EXPERIMENTAL MODEL AND SUBJECT DETAILS
  - Cell culture
- METHOD DETAILS
  - Stable and transient protein expression
  - Treatment with siRNA
  - Gene disruption
  - Immunoblot analysis
  - Local UVC stimulation by three-photon absorption
  - Fluorescence recovery after photobleaching
  - Local UVC irradiation with isopore membrane filters
  - Immunofluorescence staining
  - Assessment of H3K27ac and HaloTag 7-fusion proteins at LUD sites
  - Assessment of chromocenter localization of EGFP-XPC in MEFs
  - LacO-LacR tethering assay
  - Preparation of recombinant proteins
  - NER dual incision assay
  - GST pull-down assay
  - Peptide pull-down assay
  - Assessment of the *in vivo* repair rate of UV-induced 6-4PPs
- QUANTIFICATION AND STATISTICAL ANALYSIS

SUPPLEMENTAL INFORMATION

Supplemental information can be found online at https://doi.org/10.1016/j.isci.2022.104040.

ACKNOWLEDGMENTS

We thank Prof. Shigenori Iwai (Graduate School of Engineering Science, Osaka University) for providing us with the oligonucleotide containing a 6-4PP used for *in vitro* NER assays. The authors are grateful also to the members of the Biosignal Research Center, Kobe University, and the Department of Biology, Graduate School of Science, Kobe University for helpful discussions and encouragement. This work was supported by Grants-in-Aid (KAKENHI) to K.S. (Grant Number JP16H06307 and JP21H03598) and to M.K. (Grant Number JP21K17889).

AUTHOR CONTRIBUTIONS

M.K. and K.S. conceived the study, designed the experiments, and prepared the manuscript with input from all co-authors. M.K., F.K., T.Maeda, K.K., and A.K. performed the experiments to analyze the roles

of HDACs and MTAs in XPC recruitment and histone deacetylation induced by local UV damage. M.K. and E.K. examined XPC localization in mouse cells. M.K. also conducted the analyses of the XPC-M region using *in vitro* and *in vivo* assays. K.T. set up the LacO-LacR tethering system, and performed experiments and data analysis. H.T. conducted *in vitro* NER assays. T.Y. and T.Matsuda contributed to analyses of acetylated histone H3 peptides. M.N. provided us with a construct for expression of DsRed-HP1α and helped with data analysis. M.Y. and W.S. discussed all the results and provided supporting studies.

DECLARATION OF INTERESTS

The authors declare no competing interests.

Received: September 3, 2021
Revised: February 7, 2022
Accepted: March 4, 2022
Published: April 15, 2022

REFERENCES

Adam, S., Dabin, J., Chevallier, O., Leroy, O., Baldeyron, C., Corpet, A., Lomonte, P., Renaud, O., Almouzni, G., and Polo, S.E. (2016). Real-time tracking of parental histones reveals their contribution to chromatin integrity following DNA damage. Mol. Cell *64*, 65–78.

Akita, M., Tak, Y.-S., Shimura, T., Matsumoto, S., Okuda-Shimizu, Y., Shimizu, Y., Nishi, R., Saitoh, H., Iwai, S., Mori, T., et al. (2015). SUMOylation of xeroderma pigmentosum group C protein regulates DNA damage recognition during nucleotide excision repair. Sci. Rep. *5*, 10984.

Anantharaman, V. (2001). Peptide-N-glycanases and DNA repair proteins, Xp-C/Rad4, are, respectively, active and inactivated enzymes sharing a common transglutaminase fold. Hum. Mol. Genet. *10*, 1627–1630.

Batty, D., Rapic'-Otrin, V., Levine, A.S., and Wood, R.D. (2000). Stable binding of human XPC complex to irradiated DNA confers strong discrimination for damaged sites. J. Mol. Biol. *300*, 275–290.

Bunick, C.G., Miller, M.R., Fuller, B.E., Fanning, E., and Chazin, W.J. (2006). Biochemical and structural domain analysis of xeroderma pigmentosum complementation group C protein. Biochemistry *45*, 14965–14979.

Burgess, R.C., Burman, B., Kruhlak, M.J., and Misteli, T. (2014). Activation of DNA damage response signaling by condensed chromatin. Cell. Rep. *9*, 1703–1717.

Cattoglio, C., Zhang, E.T., Grubisic, I., Chiba, K., Fong, Y.W., and Tjian, R. (2015). Functional and mechanistic studies of XPC DNA-repair complex as transcriptional coactivator in embryonic stem cells. Proc. Natl. Acad. Sci. U S A *112*, E2317–E2326.

Chavanne, F., Broughton, B.C., Pietra, D., Nardo, T., Browitt, A., Lehmann, A.R., and Stefanini, M. (2000). Mutations in the XPC gene in families with xeroderma pigmentosum and consequences at the cell, protein, and transcript levels. Cancer Res. *60*, 1974–1982.

Chen, X., Velmurugu, Y., Zheng, G., Park, B., Shim, Y., Kim, Y., Liu, L., Houten, B.V., He, C., Ansari, A., et al. (2015). Kinetic gating mechanism of DNA damage recognition by Rad4/XPC. Nat. Commun. *6*, 5849.

Cheon, N.Y., Kim, H.-S., Yeo, J.-E., Schärer, O.D., and Lee, J.Y. (2019). Single-molecule visualization reveals the damage search mechanism for the human NER protein XPC-RAD23B. Nucleic Acids Res. *47*, 8337–8347.

Chu, G., and Chang, E. (1988). Xeroderma pigmentosum group E cells lack a nuclear factor that binds to damaged DNA. Science *242*, 564–567.

Datta, A., Bagchi, S., Nag, A., Shiyanov, P., Adami, G.R., Yoon, T., and Raychaudhuri, P. (2001). The p48 subunit of the damaged-DNA binding protein DDB associates with the CBP/p300 family of histone acetyltransferase. Mutat. Res. *486*, 89–97.

DiGiovanna, J.J., and Kraemer, K.H. (2012). Shining a light on xeroderma pigmentosum. J. Invest. Dermatol. *132*, 785–796.

Fei, J., Kaczmarek, N., Luch, A., Glas, A., Carell, T., and Naegeli, H. (2011). Regulation of nucleotide excision repair by UV-DDB: prioritization of damage recognition to internucleosomal DNA. PLoS Biol. *9*, 2217.

Fischer, E.S., Scrima, A., Böhm, K., Matsumoto, S., Lingaraju, G.M., Faty, M., Yasuda, T., Cavadini, S., Wakasugi, M., Hanaoka, F., et al. (2011). The molecular basis of CRL4DDB2/CSA ubiquitin ligase architecture, targeting, and activation. Cell *147*, 1024–1039.

Fitch, M.E., Nakajima, S., Yasui, A., and Ford, J.M. (2003). *In vivo* recruitment of XPC to UV-induced cyclobutane pyrimidine dimers by the DDB2 gene product. J. Biol. Chem. *278*, 46906–46910.

Fujiwara, Y., Masutani, C., Mizukoshi, T., Kondo, J., Hanaoka, F., and Iwai, S. (1999). Characterization of DNA recognition by the human UV-damaged DNA-binding protein. J. Biol. Chem. *274*, 20027–20033.

Geiger, T., Wehner, A., Schaab, C., Cox, J., and Mann, M. (2012). Comparative proteomic analysis of eleven common cell lines reveals ubiquitous but varying expression of most proteins. Mol. Cell. Proteomics *11*, M111.014050.

Gillet, L.C.J., and Schärer, O.D. (2006). Molecular mechanisms of mammalian global genome nucleotide excision repair. Chem. Rev. *106*, 253–276.

Groisman, R., Polanowska, J., Kuraoka, I., Sawada, J., Saijo, M., Drapkin, R., Kisselev, A.F., Tanaka, K., and Nakatani, Y. (2003). The ubiquitin ligase activity in the DDB2 and CSA complexes is differentially regulated by the COP9 signalosome in response to DNA damage. Cell *113*, 357–367.

Guenatri, M., Bailly, D., Maison, C., and Almouzni, G. (2004). Mouse centric and pericentric satellite repeats form distinct functional heterochromatin. J. Cell Biol. *166*, 493–505.

Hara, R., Mo, J., and Sancar, A. (2000). DNA damage in the nucleosome core is refractory to repair by human excision nuclease. Mol. Cell. Biol. *20*, 9173–9181.

Hassig, C.A., Tong, J.K., Fleischer, T.C., Owa, T., Grable, P.G., Ayer, D.E., and Schreiber, S.L. (1998). A role for histone deacetylase activity in HDAC1-mediated transcriptional repression. Proc. Natl. Acad. Sci. U S A *95*, 3519–3524.

Hwang, B.J., Ford, J.M., Hanawalt, P.C., and Chu, G. (1999). Expression of the p48 xeroderma pigmentosum gene is p53-dependent and is involved in global genomic repair. Proc. Natl. Acad. Sci. U S A *96*, 424–428.

Kakumu, E., Nakanishi, S., Shiratori, H.M., Kato, A., Kobayashi, W., Machida, S., Yasuda, T., Adachi, N., Saito, N., Ikura, T., et al. (2017). Xeroderma pigmentosum group C protein interacts with histones: regulation by acetylated states of histone H3. Genes Cells *22*, 310–327.

Kapetanaki, M.G., Guerrero-Santoro, J., Bisi, D.C., Hsieh, C.L., Rapić-Otrin, V., and Levine, A.S. (2006). The DDB1-CUL4ADDB2 ubiquitin ligase is deficient in xeroderma pigmentosum group E and targets histone H2A at UV-damaged DNA sites. Proc. Natl. Acad. Sci. U S A *103*, 2588–2593.

Keeney, S., Chang, G.J., and Linn, S. (1993). Characterization of a human DNA damage binding protein implicated in xeroderma pigmentosum E. J. Biol. Chem. *268*, 21293–21300.

Kong, M., Liu, L., Chen, X., Driscoll, K.I., Mao, P., Böhm, S., Kad, N.M., Watkins, S.C., Bernstein,

K.A., Wyrick, J.J., et al. (2016). Single-molecule imaging reveals that Rad4 employs a dynamic DNA damage recognition process. Mol. Cell *64*, 376–387.

Krumm, A., Barckhausen, C., Kücük, P., Tomaszowski, K.-H., Loquai, C., Fahrer, J., Krämer, O.H., Kaina, B., and Roos, W.P. (2016). Enhanced histone deacetylase activity in malignant melanoma provokes RAD51 and FANCD2-triggered drug resistance. Cancer Res. *76*, 3067–3077.

Kusakabe, M., Onishi, Y., Tada, H., Kurihara, F., Kusao, K., Furukawa, M., Iwai, S., Yokoi, M., Sakai, W., and Sugasawa, K. (2019). Mechanism and regulation of DNA damage recognition in nucleotide excision repair. Genes Environ. *41*, 2.

Kusumoto, R., Masutani, C., Sugasawa, K., Iwai, S., Araki, M., Uchida, A., Mizukoshi, T., and Hanaoka, F. (2001). Diversity of the damage recognition step in the global genomic nucleotide excision repair *in vitro*. Mutat. Res. *485*, 219–227.

Liu, J., Gu, J., Feng, Z., Yang, Y., Zhu, N., Lu, W., and Qi, F. (2016). Both HDAC5 and HDAC6 are required for the proliferation and metastasis of melanoma cells. J. Transl. Med. *14*, 7.

Luijsterburg, M.S., Lindh, M., Acs, K., Vrouwe, M.G., Pines, A., van Attikum, H., Mullenders, L.H., and Dantuma, N.P. (2012). DDB2 promotes chromatin decondensation at UV-induced DNA damage. J. Cell Biol. *197*, 267–281.

Marteijn, J.A., Lans, H., Vermeulen, W., and Hoeijmakers, J.H. (2014). Understanding nucleotide excision repair and its roles in cancer and ageing. Nat. Rev. Mol. Cell Biol. *15*, 465–481.

Martinez, E., Palhan, V.B., Tjernberg, A., Lymar, E.S., Gamper, A.M., Kundu, T.K., Chait, B.T., and Roeder, R.G. (2001). Human STAGA complex is a chromatin-acetylating transcription coactivator that interacts with pre-mRNA splicing and DNA damage-binding factors *in vivo*. Mol. Cell Biol. *21*, 6782–6795.

Matsumoto, S., Cavadini, S., Bunker, R.D., Grand, R.S., Potenza, A., Rabl, J., Yamamoto, J., Schenk, A.D., Schübeler, D., Iwai, S., et al. (2019). DNA damage detection in nucleosomes involves DNA register shifting. Nature *571*, 79–84.

Matsunuma, R., Niida, H., Ohhata, T., Kitagawa, K., Sakai, S., Uchida, C., Shiotani, B., Matsumoto, M., Nakayama, K.I., Ogura, H., et al. (2016). UV damage-induced phosphorylation of HBO1 triggers CRL4DDB2-mediated degradation to regulate cell proliferation. Mol. Cell Biol. *36*, 394–406.

May, N.L., Mota-Fernandes, D., Vélez-Cruz, R., Iltis, I., Biard, D., and Egly, J.M. (2010). NER factors are recruited to active promoters and facilitate chromatin modification for transcription in the absence of exogenous genotoxic attack. Mol. Cell *38*, 54–66.

Meldrum, R.A., Botchway, S.W., Wharton, C.W., and Hirst, G.J. (2003). Nanoscale spatial induction of ultraviolet photoproducts in cellular DNA by three-photon near-infrared absorption. EMBO Rep. *4*, 1144–1149.

Milazzo, G., Mercatelli, D., Muzio, G.D., Triboli, L., Rosa, P.D., Perini, G., and Giorgi, F.M. (2020). Histone deacetylases (HDACs): evolution, specificity, role in transcriptional complexes, and pharmacological actionability. Genes *11*, 556.

Millard, C.J., Fairall, L., and Schwabe, J.W.R. (2014). Towards an understanding of the structure and function of MTA1. Cancer Metast. Rev. *33*, 857–867.

Millard, C.J., Watson, P.J., Celardo, I., Gordiyenko, Y., Cowley, S.M., Robinson, C.V., Fairall, L., and Schwabe, J.W.R. (2013). Class I HDACs share a common mechanism of regulation by inositol phosphates. Mol. Cell *51*, 57–67.

Miller, R.D., Prakash, L., and Prakash, S. (1982). Defective excision of pyrimidine dimers and interstrand DNA crosslinks in rad7 and rad23 mutants of Saccharomyces cerevisiae. Mol. Gen. Genet. *188*, 235–239.

Min, J.-H., and Pavletich, N.P. (2007). Recognition of DNA damage by the Rad4 nucleotide excision repair protein. Nature *449*, 570–575.

Moser, J., Volker, M., Kool, H., Alekseev, S., Vrieling, H., Yasui, A., Zeeland, A.A.V., and Mullenders, L.H.F. (2005). The UV-damaged DNA binding protein mediates efficient targeting of the nucleotide excision repair complex to UV-induced photo lesions. DNA Repair *4*, 571–582.

Naf, D., Kupfer, G.M., Suliman, A., Lambert, K., and D'Andrea, A.D. (1998). Functional activity of the fanconi anemia protein FAA requires FAC binding and nuclear localization. Mol. Cell. Biol. *18*, 5952–5960.

Nishi, R., Alekseev, S., Dinant, C., Hoogstraten, D., Houtsmuller, A.B., Hoeijmakers, J.H.J., Vermeulen, W., Hanaoka, F., and Sugasawa, K. (2009). UV-DDB-dependent regulation of nucleotide excision repair kinetics in living cells. DNA Repair *8*, 767–776.

Nishi, R., Okuda, Y., Watanabe, E., Mori, T., Iwai, S., Masutani, C., Sugasawa, K., and Hanaoka, F. (2005). Centrin 2 stimulates nucleotide excision repair by interacting with xeroderma pigmentosum group C protein. Mol. Cell. Biol. *25*, 5664–5674.

Nishi, R., Sakai, W., Tone, D., Hanaoka, F., and Sugasawa, K. (2013). Structure-function analysis of the EF-hand protein centrin-2 for its intracellular localization and nucleotide excision repair. Nucleic Acids Res. *41*, 6917–6929.

Nishigori, C., and Sugasawa, K. (2019). DNA Repair Disorders (Springer Nature).

Nishimoto, K., Niida, H., Uchida, C., Ohhata, T., Kitagawa, K., Motegi, A., Suda, T., and Kitagawa, M. (2020). HDAC3 is required for XPC recruitment and nucleotide excision repair of DNA damage induced by UV irradiation. Mol. Cancer Res. *18*, 1367–1378.

Okuda, M., Kinoshita, M., Kakumu, E., Sugasawa, K., and Nishimura, Y. (2015). Structural insight into the mechanism of TFIIH recognition by the acidic string of the nucleotide excision repair factor XPC. Structure *23*, 1827–1837.

Okuda, Y., Nishi, R., Ng, J.M.Y., Vermeulen, W., van der Horst, G.T.J., Mori, T., Hoeijmakers, J.H.J., Hanaoka, F., and Sugasawa, K. (2004). Relative levels of the two mammalian Rad23 homologs determine composition and stability of the xeroderma pigmentosum group C protein complex. DNA Repair *3*, 1285–1295.

Osakabe, A., Tachiwana, H., Kagawa, W., Horikoshi, N., Matsumoto, S., Hasegawa, M., Matsumoto, N., Toga, T., Yamamoto, J., Hanaoka, F., et al. (2015). Structural basis of pyrimidine-pyrimidone (6-4) photoproduct recognition by UV-DDB in the nucleosome. Sci. Rep. *5*, 16330.

Paetkau, D.W., Riese, J.A., MacMorran, W.S., Woods, R.A., and Gietz, R.D. (1994). Interaction of the yeast RAD7 and SIR3 proteins: implications for DNA repair and chromatin structure. Genes Dev. *8*, 2035–2045.

Payne, A., and Chu, G. (1994). Xeroderma pigmentosum group E binding factor recognizes a broad spectrum of DNA damage. Mutat. Res. *310*, 89–102.

Pines, A., Vrouwe, M.G., Marteijn, J.A., Typas, D., Luijsterburg, M.S., Cansoy, M., Hensbergen, P., Deelder, A., de Groot, A., Matsumoto, S., et al. (2012). PARP1 promotes nucleotide excision repair through DDB2 stabilization and recruitment of ALC1. J. Cell Biol. *199*, 235–249.

Pogliano, C.B., Gatti, M., Rüthemann, P., Garajovà, Z., Penengo, L., and Naegeli, H. (2017). ASH1L histone methyltransferase regulates the handoff between damage recognition factors in global-genome nucleotide excision repair. Nat. Commun. *8*, 1333.

Polo, S.E., and Almouzni, G. (2015). Chromatin dynamics after DNA damage: the legacy of the access-repair-restore model. DNA Repair *36*, 114–121.

Puumalainen, M.-R., Lessel, D., Rüthemann, P., Kaczmarek, N., Bachmann, K., Ramadan, K., and Naegeli, H. (2014). Chromatin retention of DNA damage sensors DDB2 and XPC through loss of p97 segregase causes genotoxicity. Nat. Commun. *5*, 3695.

Rapić-Otrin, V., McLenigan, M.P., Bisi, D.C., Gonzalez, M., and Levine, A.S. (2002). Sequential binding of UV DNA damage binding factor and degradation of the p48 subunit as early events after UV irradiation. Nucleic Acids Res. *30*, 2588–2598.

Rapić-Otrin, V., Navazza, V., Nardo, T., Botta, E., McLenigan, M., Bisi, D.C., Levine, A.S., and Stefanini, M. (2003). True XP group E patients have a defective UV-damaged DNA binding protein complex and mutations in DDB2 which reveal the functional domains of its p48 product. Hum. Mol. Genet. *12*, 1507–1522.

Reardon, J.T., Nichols, A.F., Keeney, S., Smith, C.A., Taylor, J.S., Linn, S., and Sancar, A. (1993). Comparative analysis of binding of human damaged DNA-binding protein (XPE) and Escherichia coli damage recognition protein (UvrA) to the major ultraviolet photoproducts: T[c,s]T, T[t,s]T, T[6-4]T, and T[Dewar]T. J. Biol. Chem. *268*, 21301–21308.

Riedl, T., Hanaoka, F., and Egly, J.M. (2003). The comings and goings of nucleotide excision repair factors on damaged DNA. EMBO J. *22*, 5293–5303.

Robu, M., Shah, R.G., Petitclerc, N., Brind'Amour, J., Kandan-Kulangara, F., and Shah, G.M. (2013). Role of poly(ADP-ribose) polymerase-1 in the removal of UV-induced DNA lesions by nucleotide excision repair. Proc. Natl. Acad. Sci. U S A *110*, 1658–1663.

Robu, M., Shah, R.G., Purohit, N.K., Zhou, P., Naegeli, H., and Shah, G.M. (2017). Poly(ADP-ribose) polymerase 1 escorts XPC to UV-induced DNA lesions during nucleotide excision repair. Proc. Natl. Acad. Sci. U S A *114*, E6847–E6856.

Sakai, W., Yuasa-Sunagawa, M., Kusakabe, M., Kishimoto, A., Matsui, T., Kaneko, Y., Akagi, J., Huyghe, N., Ikura, M., Ikura, T., et al. (2020). Functional impacts of the ubiquitin–proteasome system on DNA damage recognition in global genome nucleotide excision repair. Sci. Rep. *10*, 19704.

Sands, A.T., Abuin, A., Sanchez, A., Conti, C.J., and Bradley, A. (1995). High susceptibility to ultraviolet-induced carcinogenesis in mice lacking XPC. Nature *377*, 162–165.

Schärer, O.D. (2013). Nucleotide excision repair in eukaryotes. Cold Spring Harb. Perspect Biol. *5*, a012609.

Schneider, C.A., Rasband, W.S., and Eliceiri, K.W. (2012). NIH Image to ImageJ: 25 years of image analysis. Nat. Methods *9*, 671–675.

Scrima, A., Konícková, R., Czyzewski, B.K., Kawasaki, Y., Jeffrey, P.D., Groisman, R., Nakatani, Y., Iwai, S., Pavletich, N.P., and Thomä, N.H. (2008). Structural basis of UV DNA-damage recognition by the DDB1-DDB2 complex. Cell *135*, 1213–1223.

Smerdon, M.J., Lan, S.Y., Calza, R.E., and Reeves, R. (1982). Sodium butyrate stimulates DNA repair in UV-irradiated normal and xeroderma pigmentosum human fibroblasts. J. Biol. Chem. *257*, 13441–13447.

Sugasawa, K. (2019). Mechanism and regulation of DNA damage recognition in mammalian nucleotide excision repair. Enzymes *45*, 99–138.

Sugasawa, K., Ng, J.M.Y., Masutani, C., Iwai, S., van der Spek, P.J., Eker, A.P.M., Hanaoka, F., Bootsma, D., and Hoeijmakers, J.H.J. (1998). Xeroderma pigmentosum group C protein complex is the initiator of global genome nucleotide excision repair. Mol. Cell *2*, 223–232.

Sugasawa, K., Okamoto, T., Shimizu, Y., Masutani, C., Iwai, S., and Hanaoka, F. (2001). A multistep damage recognition mechanism for global genomic nucleotide excision repair. Genes Dev. *15*, 507–521.

Sugasawa, K., Okuda, Y., Saijo, M., Nishi, R., Matsuda, N., Chu, G., Mori, T., Iwai, S., Tanaka, K., Tanaka, K., et al. (2005). UV-induced ubiquitylation of XPC protein mediated by UV-DDB-ubiquitin ligase complex. Cell *121*, 387–400.

Sugasawa, K., Shimizu, Y., Iwai, S., and Hanaoka, F. (2002). A molecular mechanism for DNA damage recognition by the xeroderma pigmentosum group C protein complex. DNA Repair *1*, 95–107.

Tan, T., and Chu, G. (2002). p53 binds and activates the xeroderma pigmentosum DDB2 gene in humans but not mice. Mol. Cell Biol. *22*, 3247–3254.

Tang, J., and Chu, G. (2002). Xeroderma pigmentosum complementation group E and UV-damaged DNA-binding protein. DNA Repair *1*, 601–616.

Tang, J.Y., Hwang, B.J., Ford, J.M., Hanawalt, P.C., and Chu, G. (2000). Xeroderma pigmentosum p48 gene enhances global genomic repair and suppresses UV-induced mutagenesis. Mol. Cell *5*, 737–744.

Toyooka, T., and Ibuki, Y. (2009). Histone deacetylase inhibitor sodium butyrate enhances the cell killing effect of psoralen plus UVA by attenuating nucleotide excision repair. Cancer Res. *69*, 3492–3500.

Trego, K.S., and Turchi, J.J. (2006). Pre-steady-state binding of damaged DNA by XPC–hHR23B reveals a kinetic mechanism for damage discrimination. Biochemistry *45*, 1961–1969.

Ura, K., Araki, M., Saeki, H., Masutani, C., Ito, T., Iwai, S., Mizukoshi, T., Kaneda, Y., and Hanaoka, F. (2001). ATP-dependent chromatin remodeling facilitates nucleotide excision repair of UV-induced DNA lesions in synthetic dinucleosomes. EMBO J. *20*, 2004–2014.

Verhage, R., Zeeman, A.-M., de Groot, N., Gleig, F., Bang, D.D., de Putte, P.V., and Brouwer, J. (1994). The RAD7 and RAD16 genes, which are essential for pyrimidine dimer removal from the silent mating type loci, are also required for repair of the nontranscribed strand of an active gene in Saccharomyces cerevisiae. Mol. Cell Biol. *14*, 6135–6142.

Volker, M., Moné, M.J., Karmakar, P., van Hoffen, A., Schul, W., Vermeulen, W., Hoeijmakers, J.H.J., van Driel, R., van Zeeland, A.A., and Mullenders, L.H.F. (2001). Sequential assembly of the nucleotide excision repair factors *in vivo*. Mol. Cell *8*, 213–224.

Wang, H., Zhai, L., Xu, J., Joo, H.-Y., Jackson, S., Erdjument-Bromage, H., Tempst, P., Xiong, Y., and Zhang, Y. (2006). Histone H3 and H4 ubiquitylation by the CUL4-DDB-ROC1 ubiquitin ligase facilitates cellular response to DNA damage. Mol. Cell *22*, 383–394.

Wang, Q.-E., Zhu, Q., Wani, G., Chen, J., and Wani, A.A. (2004). UV radiation-induced XPC translocation within chromatin is mediated by damaged-DNA binding protein. Carcinogenesis *25*, 1033–1043.

Wittschieben, B.Ø., Iwai, S., and Wood, R.D. (2005). DDB1-DDB2 (xeroderma pigmentosum group E) protein complex recognizes a cyclobutane pyrimidine dimer, mismatches, apurinic/apyrimidinic sites, and compound lesions in DNA. J. Biol. Chem. *280*, 39982–39989.

Xue, Y., Wong, J., Moreno, G.T., Young, M.K., Côté, J., and Wang, W. (1998). NURD, a novel complex with both ATP-dependent chromatin-remodeling and histone deacetylase activities. Mol. Cell *2*, 851–861.

Yasuda, G., Nishi, R., Watanabe, E., Mori, T., Iwai, S., Orioli, D., Stefanini, M., Hanaoka, F., and Sugasawa, K. (2007). *In vivo* destabilization and functional defects of the xeroderma pigmentosum C protein caused by a pathogenic missense mutation. Mol. Cell Biol. *27*, 6606–6614.

Yasuda, T., Kagawa, W., Ogi, T., Kato, T.A., Suzuki, T., Dohmae, N., Takizawa, K., Nakazawa, Y., Genet, M.D., Saotome, M., et al. (2018). Novel function of HATs and HDACs in homologous recombination through acetylation of human RAD52 at double-strand break sites. PLoS Genet. *14*, e1007277.

Yasuda, T., Sugasawa, K., Shimizu, Y., Iwai, S., Shiomi, T., and Hanaoka, F. (2005). Nucleosomal structure of undamaged DNA regions suppresses the non-specific DNA binding of the XPC complex. DNA Repair *4*, 389–395.

Zhang, Y., Iratni, R., Erdjument-Bromage, H., Tempst, P., and Reinberg, D. (1997). Histone deacetylases and SAP18, a novel polypeptide, are components of a human Sin3 complex. Cell *89*, 357–364.

Zhang, Y., Ng, H.-H., Erdjument-Bromage, H., Tempst, P., Bird, A., and Reinberg, D. (1999). Analysis of the NuRD subunits reveals a histone deacetylase core complex and a connection with DNA methylation. Genes Dev. *13*, 1924–1935.

Zhao, R., Han, C., Eisenhauer, E., Kroger, J., Zhao, W., Yu, J., Selvendiran, K., Liu, X., Wani, A.A., and Wang, Q.-E. (2014). DNA damage-binding complex recruits HDAC1 to repress Bcl-2 transcription in human ovarian cancer cells. Mol. Cancer Res. *12*, 370–380.

Zhu, Q., Battu, A., Ray, A., Wani, G., Qian, J., He, J., Wang, Q., and Wani, A.A. (2015). Damaged DNA-binding protein down-regulates epigenetic mark H3K56Ac through histone deacetylase 1 and 2. Mutat. Res. *776*, 16–23.

STAR★METHODS

KEY RESOURCES TABLE

REAGENT or RESOURCE	SOURCE	IDENTIFIER
Antibodies		
Mouse monoclonal anti-XPC (D-10)	Santa Cruz Biotechnology	Cat#: sc-74410; RRID: AB_1131407
Goat polyclonal anti-DDB2	R&D Systems	Cat#: AF3297; RRID: AB_2088829
Mouse monoclonal anti-α-tubulin (B-5-1-2)	Merck	Cat#: T5168; RRID: AB_477579
Mouse monoclonal anti-HDAC1 (10E2)	Cell Signaling Technology	Cat#: 5356; RRID: AB_10612242
Mouse monoclonal anti-HDAC2 (3F3)	Cell Signaling Technology	Cat#: 5113; RRID: AB_10624871
Mouse monoclonal anti-HDAC3 (7G6C5)	Cell Signaling Technology	Cat#: 3949; RRID: AB_2118371
Rabbit monoclonal abti-HDAC8	Abcam	Cat#: ab187139; RRID: AB_2715505
Mouse monoclonal anti-MTA1 (E-12)	Santa Cruz Biotechnology	Cat#: sc-373765; RRID: AB_10917039
Mouse monoclonal anti-MTA2 (F-9)	Santa Cruz Biotechnology	Cat#: sc-55566; RRID: AB_831564
Mouse monoclonal anti-MTA3 (428C2a)	Santa Cruz Biotechnology	Cat#: sc-81325; RRID: AB_1126372
Mouse monoclonal anti-trimethyl histone H3 (Lys9) (MABI0308)	Fujifilm Wako Pure Chemical	Cat#: 301-34833
Mouse monoclonal anti-acetyl histone H3 (Lys27) (MABI0309)	Fujifilm Wako Pure Chemical	Cat#: 308-34843
Rabbit polyclonal anti-histone H3 (pan-H3)	Abcam	Cat#: ab1791; RRID: AB_302613
Mouse monoclonal anti-acetylated lysine (Ac-K-103)	Cell Signaling Technology	Cat#: 9681; RRID: AB_331799
Rabbit polyclonal anti-HP1α	BioAcademia	Cat#: 70-221
Mouse monoclonal anti-6-4PPs (64M-2)	Cosmo Bio	Cat#: NM-DND-002; RRID: AB_1962842
Mouse monoclonal anti-DYKDDDDK (FLAG) tag (1E6)	Fujifilm Wako Pure Chemical	Cat#: 012-22384; RRID: AB_10660291
Mouse monoclonal anti-HA tag	Medical & Biological Laboratories	Cat#: M180-3; RRID: AB_10951811
Mouse monoclonal anti-GST (B-14)	Santa Cruz Biotechnology	Cat#: sc-138; RRID: AB_627677
Rabbit polyclonal anti-mCherry	Abcam	Cat#: ab167453; RRID: AB_2571870
Goat anti-mouse IgG (H+L) secondary antibody (Fab'), HRP-conjugated	Medical & Biological Laboratories	Cat#: 330;
Goat anti-rabbit IgG (H+L) secondary antibody (Fab'), HRP-conjugated	Medical & Biological Laboratories	Cat#: 458
Rabbit anti-goat IgG (H+L) secondary antibody (Fab'), HRP-conjugated	Medical & Biological Laboratories	Cat#: 546
Goat anti-mouse IgG (H+L) secondary antibody, Alexa Fluor 405-conjugated	Thermo Fisher Scientific	Cat#: A-31553; RRID: AB_221604
Goat anti-mouse IgG (H+L) secondary antibody (Fab'), Alexa Fluor 594-conjugated	Thermo Fisher Scientific	Cat#: A-11020; RRID: AB_2534087
Goat anti-rabbit IgG (H+L) secondary antibody, Alexa Fluor 594-conjugated	Thermo Fisher Scientific	Cat#: A-11037; RRID: AB_2534095
Bacterial and virus strains		
Escherichia coli strain: BL21 (DE3)	Merck	Cat#: 69450
Escherichia coli strain: DH10Bac	Thermo Fisher Scientific	Cat#: 10361012
Recombinant baculovirus expressing FLAG-XPC^{WT}	Nishi et al., 2005	N/A
Recombinant baculovirus expressing FLAG-XPC$^{\Delta M}$, FLAG-XPC-M	This paper	N/A
Recombinant retrovirus expressing FLAG-EGFP-XPC (WT, NLS-ΔN, ΔM, ΔC, NLS-M)	This paper	N/A

(*Continued on next page*)

Continued

REAGENT or RESOURCE	SOURCE	IDENTIFIER
Chemicals, peptides, and recombinant proteins		
Trichostatin A	Fujifilm Wako Pure Chemical	203-17561; CAS: 58880-19-6
Romidepsin	Cayman Chemical	17130; CAS: 128517-07-7
Leupeptin hemisulfate	Merck	11 017 101 001; CAS: 103476-89-7
Aprotinin	Merck	10 236 624 001; CAS: 9087-70-1
Pepstatin	Merck	11 359 053 001; CAS: 26305-03-3
Pefabloc SC (AEBSF)	Merck	11 429 868 001; CAS: 30827-99-7
Acetyl-CoA (lithium salt)	Merck	A2181; CAS: 32140-51-5
ImmunoStar LD (chemiluminescence substrate)	Fujifilm Wako Pure Chemical	290-69904
ImmunoStar Zeta (chemiluminescence substrate)	Fujifilm Wako Pure Chemical	295-72404
FuGENE HD transfection reagent	Promega	Cat#: E2311
HaloTag TMR ligand	Promega	Cat#: G8251
Lipofectamine RNAiMAX transfection reagent	Thermo Fisher Scientific	Cat#: 13778150
Histone H3 (1-21)-GGK (biotin)-NH_2 peptide	Anaspec	Cat#: AS-61702
Histone H3 K27 peptide - biotinylated	Active Motif	Cat#: 81048
Histone H3 K27ac peptide – biotinylated	Active Motif	Cat#: 81049
Glutathione Sepharose 4 Fast Flow	Cytiva	Cat#: 17 513 201
Dynabeads Protein G	Thermo Fisher Scientific	Cat#: 10003D
FG beads Streptavidin	Tamagawa Seiki	Cat#: TAS8848N1170
Critical commercial assays		
GeneArt CRISPR nuclease vector with CD4 enrichment kit	Thermo Fisher Scientific	Cat#: A21175
SE cell line 4D-Nucleofector X kit S	Lonza	Cat# V4XC-1032
Experimental models: Cell lines		
Human: U2OS cell lines (WT, DDB2 KO, XPC KO)	Sakai et al., 2020	N/A
Human: U2OS cells stably expressing FLAG-EGFP-XPC^{WT}	Sakai et al., 2020	N/A
Human: $U2OS^{DDB2\ KO}$ cells stably expressing FLAG-EGFP-XPC^{WT}	This paper	N/A
Human: $U2OS^{DKO}$ cells	This paper	N/A
Human: $U2OS^{DKO}$ cells stably expressing FLAG-EGFP-XPC^{WT}	This paper	N/A
Human: $U2OS^{DKO}$ cells stably expressing FLAG-EGFP-$XPC^{\Delta M}$	This paper	N/A
Human: U2OS-LacO-I-SceI-TetO cells	Burgess et al., 2014	Kerafast: ENH105-FP
Human: U2OS-LacO-I-SceI-TetO/FLAG-EGFP-XPC^{WT} cells	This paper	N/A
Mouse: *Xpc*-deficient mouse embryonic fibroblast cells (MEFs)	Sands et al., 1995; Okuda et al., 2004	N/A
Mouse: Xpc-deficient MEFs stably expressing FLAG-EGFP-XPC and DsRed-HP1α	This paper	N/A
Mouse: *Xpc*-deficient MEFs stably expressing FLAG-EGFP-XPC (WT or mutant)	This paper	N/A
Oligonucleotides		
siRNA targeting sequences: listed in Table S1	This paper	N/A
siRNA targeting HDAC2	Thermo Fisher Scientific	Cat#: s6495
siRNA targeting MTA1	Thermo Fisher Scientific	Cat#: s17390
siRNA targeting MTA2	Thermo Fisher Scientific	Cat#: s17629

(*Continued on next page*)

Continued

REAGENT or RESOURCE	SOURCE	IDENTIFIER
siRNA targeting MTA3	Thermo Fisher Scientific	Cat#: s33172
AllStars Negative Control siRNA	Qiagen	Cat#: 1027281
Mission siRNA Universal Negative Control #1	Merck	Cat#: SIC001
Stealth RNAi siRNA Negative Control Lo GC	Thermo Fisher Scientific	Cat#: 12935200
Recombinant DNA		
pIREShyg	Clontech	Cat#: 6061-1
pIREShyg/FLAG-EGFP-XPC^{WT}	Nishi et al., 2009	N/A
pIREShyg/FLAG-EGFP-XPC$^{\Delta M}$	This paper	N/A
pIREShyg/HDAC1-HA	This paper	N/A
pIRESpuro2	Clontech	Cat#: 6937-1
pIRESpuro2/FLAG-EGFP-XPC^{WT}	This paper	N/A
pIRESpuro2/HDAC1-EGFP-HA	This paper	N/A
pIRESpuro2/HDAC2-EGFP-HA	This paper	N/A
pIRESneo3	Takara Bio	Cat#: 6316-21
pIRESneo3/HDAC1-FLAG-mCherry-LacR-NLS	This paper	N/A
pIRESneo3/HDAC2 (WT, H142A, siR)-FLAG-mCherry-LacR-NLS	This paper	N/A
pIRESneo3/HDAC3-FLAG-mCherry-LacR-NLS	This paper	N/A
pFC14K	Promega	Cat#: G9661
pFC14K/HDAC1, HDAC2	This paper	N/A
pFN21K	Promega	Cat#: G2831
pFN21K/MTA1, MTA2, MTA3	This paper	N/A
pFN21K/HDAC3	This paper	N/A
pMMP-puro	Näf et al., 1998	N/A
pMMP-puro/FLAG-EGFP-XPC (WT, NLS-ΔN, ΔM, ΔC, NLS-M)	This paper	N/A
Software and algorithms		
ImageJ	Schneider et al., 2012	https://imagej.nih.gov/ij/
cellSens	Olympus	https://www.olympus-lifescience.com/en/software/cellsens/
MATLAB	MathWorks	https://www.mathworks.com/products/matlab.html
GraphPad Prism 9	GraphPad Software	https://www.graphpad.com/scientific-software/prism/

RESOURCE AVAILABILITY

Lead contact

Further information and requests for resources and reagents should be directed to and will be fulfilled by the lead contact, Kaoru Sugasawa (ksugasawa@garnet.kobe-u.ac.jp).

Materials availability

Any virus strain, cell line, and recombinant DNA generated in this study is available from the lead contact upon request.

Data and code availability

All orignal data reported in this paper will be shared by the lead contact upon request.

This paper does not report any original code.

Any additional information required to reanalyze the data reported in this paper is available from the lead contact upon request.

EXPERIMENTAL MODEL AND SUBJECT DETAILS

Cell culture

Human osteosarcoma cell line U2OS and *Xpc*-deficient MEFs (Sands et al., 1995; Okuda et al., 2004) were cultured in Dulbecco's modified Eagle medium (DMEM) supplemented with 10% fetal bovine serum (FBS) at 37°C, 5% CO_2, and in a humidified atmosphere. U2OS-LacO-I-SceI-TetO cells (Burgess et al., 2014) were obtained from Kerafast and maintained in the culture medium containing 200 μg/mL hygromycin B.

METHOD DETAILS

Stable and transient protein expression

The bicistronic mammalian expression vector pIREShyg was used for the stable expression of FLAG-EGFP-XPC (wild type and ΔM mutant) and HDAC1-HA. For LacO-LacR tethering assays, the pIRESpuro2 vector was used for stable expression of FLAG-EGFP-XPC^{WT} in U2OS-LacO-I-SceI-TetO cells. The construct was linearized by digestion with the restriction enzyme *Dra* I and introduced into U2OS or derivative cells by electroporation with Gene Pulser II (Bio-Rad). Subconfluent cells in a 100 mm culture dish were trypsinized and collected by centrifugation (200 × g, 5 min). The cells were resuspended in 0.25 mL culture medium, mixed with the linearized expression construct (10 μg), and transferred into an electroporation cuvette with 0.2 cm electrode gap. Electroporation was performed by setting voltage and capacitance at 120 V and 1,070 μF, respectively. After 10 min recovery at room temperature, the cells were diluted with culture medium and incubated for 2 days. Stable transformants were then selected in the culture medium containing 200 μg/mL hygromycin B (for pIREShyg) or 1 μg/mL puromycin (for pIRESpuro2). Single clones were isolated by limiting dilution.

The retroviral expression vector pMMP-puro was used for stable expression of FLAG-EGFP-tagged human XPC derivatives in *Xpc*-deficient MEFs. Because the XPC mutants lacking the N-terminus (ΔN and M) failed to localize within the nucleus, the nuclear localization signal (NLS) of SV40 large T antigen (PKKKRKVEDP) was inserted between the EGFP and XPC sequences for these two mutants. Production of recombinant retroviruses, infection of cells, and selection of stable transformants were performed as described previously (Akita et al., 2015).

For transient protein expression with the plasmid-based DNA constructs, typically 1 × 10^5 cells were seeded in a 35 mm culture dish one day before transfection. The expression construct (2 μg) was mixed with 6 μL FuGENE HD reagent in 100 μL Opti-MEM I reduced-serum medium, incubated for 5 min at room temperature, and transferred into the dish containing the cells. The transfected cells were used for assays after incubation for 2 days. For the rescue experiments in Figures S4E and S4F, the 4D-Nucleofector system (Lonza) was used to express siRNA-resistant HDAC2-Halo. Typically, 2 × 10^5 cells were collected by centrifugation (900 × g, 10 min) and resuspended in the SE 4D-Nucleofector-X solution (20 μL) containing 0.5 μg of the expression construct. Electroporation was performed using a 16-well Nucleocuvette strip and the preset program CM-104. The cells were then diluted with the culture medium, transferred into 35 mm glass bottom dish (MatTek Corporation), and incubated at 37°C overnight. To visualize the HaloTag 7-fusion proteins, the cells were cultured for 30 min in the presence of 10 μM HaloTag TMR ligand. After the unincorporated HaloTag ligand was washed out, the cells were further cultured for at least 30 min before examination with the confocal laser scanning microscope.

Treatment with siRNA

For typical experiments, 1 × 10^5 cells were seeded in a 35 mm culture dish one day before transfection. siRNA (40 pmol) was mixed with 3 μL Lipofectamine RNAiMAX reagent in 0.5 mL Opti-MEM I reduced-serum medium, incubated for 5 min at room temperature, and transferred into the dish containing the cells with 1.5 mL culture medium (final siRNA concentration: 20 nM). For simultaneous depletion of MTA proteins, siRNA targeting each MTA was used at a final concentration of 10 nM, and the total siRNA concentration was adjusted at 30 nM by adding negative control siRNA, if only one or two MTAs were targeted. Double knockdown of HDAC1/2 was performed with 20 nM siHDAC1 #1 and 10 nM siHDAC2 (siHDAC1 #1 was used for most experiments, whereas LacO-LacR tethering assays were performed with siHDAC1 #2). In these cases, the amount of Lipofectamine RNAiMAX was increased proportionally

(4.5 μL). The transfected cells were cultured for 2 days (HDACs) or 3 days (DDB2, MTAs, and Suv39h1/2) before being used in further experiments.

AllStars Negative Control siRNA was used as a negative control in most experiments, whereas Mission siRNA Universal Negative Control #1 was used only for LacO-LacR tethering assays. When HDAC2 was depleted with Stealth RNAi siRNA, the corresponding negative control (Stealth RNAi siRNA Negative Control Lo GC) was used. To generate HDAC2 that is resistant to siRNA (s6495; Thermo Fisher Scientific), 17 silent mutations were introduced from Lys9 to Tyr25 as follows, according to the manufacturer's information that this siRNA targets the junction between exons 1 and 2.

original: AAA AAA AAA GTC TGC TAC TAC TAC GAC GGT GAT ATT GGA AAT TAT TAT TAT

siR: AAG AAG AAG GTA TGT TAT TAT TAT GAT GGA GAC ATA GGT AAC TAC TAC TAC

Gene disruption

Disruption of endogenous *DDB2* or *XPC* gene in U2OS cells was carried out in our previous study (Sakai et al., 2020), with the plasmid-based constructs co-expressing the Cas9 protein and sgRNA (using the GeneArt CRISPR nuclease vector with CD4; Thermo Fisher Scientific). To generate *DDB2/XPC*-double knockout (DKO) cells, the *XPC* gene in the previously established *DDB2*-deficient U2OS cells was disrupted with the same construct. Isolated clones were examined by immunoblot analyses, and biallelic disruption was confirmed by sequencing of the genomic DNA.

Immunoblot analysis

To prepare cell extracts, cells were lysed for 60 min on ice with modified cytoskeleton (CSK) buffer (10 mM PIPES-NaOH [pH 6.8], 3 mM $MgCl_2$, 1 mM EGTA, 0.3 M NaCl, 10% glycerol, 0.1% Triton X-100) containing a protease inhibitor cocktail (1 μg/mL leupeptin, 2 μg/mL aprotinin, 1 μg/mL pepstatin, and 50 μg/mL Pefabloc SC). Proteins were separated by SDS-PAGE and transferred onto polyvinylidene difluoride membranes. After blocking with 5% skimmed milk in TBS-T (50 mM Tris-HCl [pH 8.0], 150 mM NaCl, 0.1% Tween 20), the membranes were incubated with primary antibody diluted in the blocking solution. After washing with TBS-T, the membranes were incubated with the appropriate horseradish peroxidase-conjugated secondary antibody. Immunoreactive bands were visualized by chemiluminescence with the ImmunoStar Zeta or ImmunoStar LD reagent as a substrate. The lumino-imaging analyzer LAS-3000 (Fujifilm) and the accompanying software Image Gauge were used for the detection and quantification of chemiluminescence.

Local UVC stimulation by three-photon absorption

UV-induced photolesions were generated by using a customized confocal laser scanning fluorescence microscope system (FV3000; Olympus) equipped with a 780 nm femtosecond fiber laser (CFL; Calmar Laser) as described previously (Sakai et al., 2020). Cells expressing fluorescently labeled proteins were cultured in 35 mm glass bottom dishes. Under the confocal laser scanning microscope, a region of interest (ROI) was set within the nucleus and stimulated five times with the 780 nm femtosecond laser at ~24 mW. Fluorescence images were acquired every 5 s, and data analyses were carried out as described previously (Sakai et al., 2020).

Fluorescence recovery after photobleaching

Cells expressing EGFP-XPC (wild-type or mutant) were cultured in 35 mm glass bottom dishes. Under the confocal laser scanning microscope, a ROI was set within the nucleus, and EGFP fluorescence was bleached with the 488 nm laser at 100% power. After photobleaching, fluorescent images were acquired every 1 s, and data analyses were carried out as described previously (Sakai et al., 2020).

Local UVC irradiation with isopore membrane filters

Cells were cultured in 35 mm glass bottom dishes. After removal of the medium and wash with phosphate-buffered saline (PBS), the cells on the glass bottom were covered with a polycarbonate isopore membrane filter (5 μm pore size) and irradiated with UVC at 400 J/m^2 under a germicidal lamp with a peak wavelength of 254 nm (GL-15; Toshiba). The filter was removed, and the cells were further cultured in replenished medium at 37°C for the indicated time period.

Immunofluorescence staining

Immunofluorescence staining of histone modifications was performed essentially as described previously (Kakumu et al., 2017), with some modifications. The cells were washed twice with PBS and fixed for 10 min at room temperature with 2% paraformaldehyde in PBS. The cells were washed twice with PBS and permeabilized on ice for 10 min with PBS containing 0.1% Triton X-100. After two washes with PBS, the cells were incubated at 37°C for 30 min with 20% FBS in PBS to block non-specific antibody binding. The cells were then washed twice with PBS and incubated overnight at 4°C with the primary antibody (diluted at 1 μg/mL with 5% FBS in PBS). To confirm specificity of anti-H3K27ac staining (Figure S3B), biotinylated histone H3 K27 or K27ac peptide (Active Motif) was included in the primary antibody solution as a competitor at a final concentration of 10 μg/mL. The cells were washed five times with PBS and further incubated at 37°C for 30 min with Alexa Fluor 594 or 405-labeled anti-mouse IgG secondary antibody (diluted at 1:500 with 5% FBS in PBS). After washes five times with PBS, nuclear DNA was counterstained for 10 min at room temperature with PBS containing 1 μg/mL Hoechst 33342 or 4′,6-diamidino-2-phenylindole (DAPI). Finally, the cells were washed five times with PBS and mounted with Vectashield mounting medium (Vector Laboratories).

To observe localization of endogenous HDAC2, the cells were first incubated on ice for 20 min in the pre-extraction buffer (10 mM PIPES-NaOH [pH 6.8], 0.1 M NaCl, 0.3 M sucrose, 3 mM $MgCl_2$, 1 mM EGTA, and 0.5% Triton X-100). After two washes with PBS, the cells were fixed for 10 min at room temperature with 4% paraformaldehyde solution in PBS. Subsequently, the samples were treated as described above.

Assessment of H3K27ac and HaloTag 7-fusion proteins at LUD sites

Cells stably expressing EGFP-XPC were irradiated with UVC through isopore membrane filters and subjected to immunofluorescence staining with the anti-H3K27ac antibody. Fluorescent images were acquired by using the confocal laser scanning fluorescence microscope. To quantify relative H3K27ac levels at LUD sites, three ROIs were defined as follows: 1) the UVC-exposed area demarcated with the fluorescence of accumulating EGFP-XPC (D); 2) the entire nucleus (N); and 3) the area outside the cell as a background (BKG). Average fluorescence intensities per pixel were measured for these ROIs (defined as F_D, F_N, and F_{BKG}) and relative EGFP intensities at the *lacO* array (F_R) were calculated using the following formula: $F_R = (F_D - F_{BKG}) / (F_N - F_{BKG})$.

To assess the accumulation of HaloTag 7-fusion proteins, local UVC irradiation was similarly applied to the EGFP-XPC expressing cells that had been pre-labeled with the HaloTag TMR ligand. The cells were incubated on ice for 20 min in the pre-extraction buffer, washed twice with PBS, and fixed for 10 min at room temperature with 4% paraformaldehyde solution in PBS. Image acquisition and quantitative analysis were carried out as described above for H3K27ac.

Assessment of chromocenter localization of EGFP-XPC in MEFs

Xpc-deficient MEFs expressing EGFP-tagged human XPC (wild type or mutant) were cultured in 35 mm glass bottom dishes. The cells were washed with PBS, incubated on ice for 5 min in pre-extraction buffer, and fixed for 10 min at room temperature with 2% paraformaldehyde in PBS. Nuclear DNA was counterstained at room temperature for 20 min with PBS containing 1 μg/mL Hoechst 33342, and fluorescent images were acquired with the confocal laser scanning microscope. To assess localization of EGFP-XPC to chromocenters, whole nuclei were set as a ROI, and the correlation coefficient between EGFP and Hoechst 33342 fluorescence was calculated with the cellSens software (Olympus).

LacO-LacR tethering assay

For this assay, the pIRESneo3 vector was used for the transient expression of mCherry-LacR fusion proteins. To prepare the control construct, the N-terminus of mCherry was FLAG tagged, while NLS of SV40 large T antigen (with a stop codon) was fused to the C-terminus of LacR. Finally, the cDNA encoding HDAC was inserted to make a fusion with the N-terminus of FLAG-mCherry-LacR-NLS.

U2OS-LacO-I-SceI-TetO cells stably expressing EGFP-XPC were cultured in 35 mm glass bottom dishes and transfected with mCherry-LacR fusion protein expression constructs. For some experiments, siRNA was introduced into the cells 1 day before transfection. After 2 days, cells were washed with PBS, incubated on ice for 5 min in pre-extraction buffer, and fixed for 10 min at room temperature with 2%

paraformaldehyde in PBS. Fluorescent images were acquired by using the confocal laser scanning fluorescence microscope.

To quantify relative EGFP intensity at the *lacO* arrays, three ROIs were defined as follows: 1) the area of the *lacO* array demarcated with mCherry fluorescence (L); 2) the entire nucleus (N); and 3) the area outside the cell as a background (BKG). Average fluorescence intensities per pixel were measured for these ROIs (defined as F_L, F_N, and F_{BKG}) and relative EGFP intensities at the *lacO* array (F_R) were calculated using the following formula: $F_R = (F_L - F_{BKG}) / (F_N - F_{BKG})$.

Preparation of recombinant proteins

The heterodimeric complex containing FLAG-XPC (WT or ΔM) and RAD23B-His was purified as described previously (Nishi et al., 2005). For the preparation of FLAG-tagged XPC-M, recombinant baculovirus was generated using the Bac-to-Bac expression system (Thermo Fisher Scientific). Twenty 150 mm dishes of High Five cells were infected and cultured at 27°C for 3 days. The infected cells were harvested, washed twice with ice-cold PBS, and suspended in an eight-fold volume of NP lysis buffer (25 mM Tris-HCl [pH 8.0], 0.3 M NaCl, 10% glycerol, 1% Nonidet P-40) containing protease inhibitor cocktail. After incubation on ice for 30 min, the soluble fraction was obtained by centrifugation at 20,000 × g for 15 min and dialyzed against buffer A (50 mM Tris-HCl [pH 7.0], 0.1 M NaCl, 1 mM EDTA, 0.25 mM phenylmethylsulfonyl fluoride [PMSF]). Insoluble materials were removed by centrifugation at 20,000 × g for 10 min, and the clarified extract was loaded onto a HiPrep Heparin FF 16/10 column (Cytiva) equilibrated with buffer B (50 mM Tris-HCl [pH 8.0], 1 mM EDTA, 0.01% Nonidet P-40, 0.25 mM PMSF) containing 0.1 M NaCl. After an extensive wash with buffer B containing 0.1 M NaCl, bound proteins were eluted successively with buffer B containing 0.3 and 1 M NaCl. The NaCl eluates (1 M) containing FLAG-XPC-M were collected, mixed with 4 mL anti-FLAG M2 agarose beads (Merck) pre-washed with buffer B containing 1 M NaCl, and incubated overnight at 4°C with continuous rotation. Resin was packed into columns and washed thoroughly with buffer C (50 mM Tris-HCl [pH 7.0], 1 mM EDTA, 10% glycerol, 0.01% Nonidet P-40, 0.25 mM PMSF) containing 0.3 M NaCl. Bound proteins were then eluted with buffer C containing 0.3 M NaCl and 100 μg/mL FLAG peptide. The eluate was loaded onto a HiTrap SP HP column (1 mL; Cytiva) equilibrated with buffer C containing 0.3 M NaCl, and the bound proteins were eluted with a 0.3–1 M linear gradient of NaCl in buffer C. The peak fractions were frozen under liquid nitrogen and stored at −80°C.

For GST pull-down assays, the N-terminal tail of histone H3 encompassing amino acids 1–20 or 1–41 was fused to the N-terminus of GST. Mutant proteins were similarly prepared in which all lysine residues in the histone tails were changed to glutamines to simulate lysine acetylation. cDNAs encoding these GST fusion proteins, and a GST alone control, were cloned into the pET-24a vector (Merck) and introduced into *E. coli* BL21 (DE3) cells. Bacteria carrying the construct were cultured at 37°C in 1 L LB medium containing 50 μg/mL kanamycin until OD_{600} reached 0.6, and expression of the GST fusion protein was induced by the addition of isopropyl-β-D-thiogalactopyranoside at a final concentration of 0.5 mM. After further incubation at 16°C for 24 h, the cells were harvested, resuspended in 50 mL buffer D (20 mM Tris-HCl [pH 7.5], 0.5 M NaCl, 5 mM EDTA, 0.2 mM PMSF), and disrupted by sonication. The soluble fraction was obtained by centrifugation at 24,900 × g for 20 min and filtered through a Millex-SV 5.0 μm filter unit (Merck). The clarified extract was loaded onto a GSTrap HP column (1 mL; Cytiva) equilibrated with buffer D, and bound proteins were eluted with buffer D containing 10 mM reduced glutathione. The peak fractions were collected, dialyzed against buffer D containing 10% glycerol, and stored at −80°C.

NER dual incision assay

An internally ^{32}P-labeled, double-stranded circular DNA substrate containing a site-specific 6-4PP was prepared as described previously (Sugasawa et al., 2001). Cell-free NER dual incision of this substrate was reconstituted using purified recombinant proteins as described previously (Nishi et al., 2013). After incubation at 30°C for 30 min, DNA samples were purified and subjected to 10% denaturing PAGE. Detection and quantification were carried out with the Typhoon FLA 9500 biomolecular imager (Cytiva) and the accompanying ImageQuant TL software.

GST pull-down assay

GST fusion proteins (3.8 μg H3(1–20)-GST, 6.1 μg H3(1–41)-GST, or 3.0 μg GST control) were incubated on ice for 1 h with 10 μL Glutathione Sepharose 4 Fast Flow beads in 100 μL buffer E (10 mM PIPES-NaOH

[pH 6.8], 0.3 M sucrose, 3 mM $MgCl_2$, 1 mM EGTA, 0.5% Triton X-100) containing 0.15 M NaCl and 0.1 mg/mL heat-denatured bovine serum albumin (BSA). After washes three times with buffer E containing 0.15 M NaCl, the beads were incubated on ice for 1 h with 35 ng XPC-RAD23B in 50 μL buffer E containing 0.15 M NaCl and 0.1 mg/mL heat-denatured BSA. After three washes with binding buffer, bound proteins were eluted from the beads in buffer F (20 mM sodium phosphate [pH 7.8], 0.3 M NaCl, 10% glycerol, 0.1% Triton X-100) containing 10 mM reduced glutathione, and were subjected to immunoblot analyses. Binding of FLAG-XPC-M was examined as above, except the binding solution contained 0.1 M NaCl and 0.02 mg/mL acetylated BSA (Nippon Gene), rather than heat-denatured BSA. FLAG-XPC-M (25 ng) was included in each reaction.

Peptide pull-down assay

The recombinant histone acetyltransferase CBP-FLAG was purified as described previously (Yasuda et al., 2018), and used for *in vitro* acetylation of the biotinylated histone H3 tail peptides. Dynabeads Protein G (5 μL) was incubated with 3 μg anti-DYKDDDDK tag antibody in 100 μL cold PBS, washed three times with buffer G (50 mM Tris-HCl [pH 8.0], 0.3 M NaCl, 1 mM EDTA, 1 mM dithiothreitol), and incubated with 2.5 μg of CBP-FLAG on ice for 1 h in 50 μL of buffer G. To remove unbound CBP-FLAG, the beads were washed three times with buffer H (50 mM Tris-HCl [pH 8.0], 10% glycerol, 1 mM EDTA, 1 mM dithiothreitol). Beads were subsequently incubated with 8 μg histone H3 (1–21)-GGK (biotin)-NH_2 peptide (Anaspec) at 30°C for 2 h in 200 μL buffer H with or without 0.2 mg/mL acetyl-CoA to introduce acetylation into the peptide. The beads were then removed using a magnetic stand, and the recovered supernatant was used as acetylated and non-acetylated histone peptides.

To investigate the interaction with FLAG-XPC-M, 5 μL paramagnetic beads conjugated to streptavidin (FG beads Streptavidin) were incubated on ice for 1 h with the above reaction mixture (50 μL) containing the acetylated or non-acetylated histone peptide. After being washed five times with buffer E containing 0.1 M NaCl, the beads were incubated on ice for 1 h with 25 ng FLAG-XPC-M in 50 μL of buffer E containing 0.1 M NaCl and 0.02 mg/mL acetylated BSA. After the beads were washed five times with buffer E containing 0.1 M NaCl, bound proteins were eluted by denaturation in SDS sample buffer (62.5 mM Tris–HCl [pH 6.8], 1% SDS, 1% 3-mercapto-1,2-propanediol, 10% glycerol, 0.02% bromophenol blue), and subjected to SDS-PAGE and immunoblot analyses.

To confirm the acetylation of the histone peptide, we used a Waters UPLC (ACQUITY QSM) with a photodiode array detector and a quadrupole tandem mass spectrometer (XEVO-TQS). The UPLC separation was performed on a Waters ODS column ACQUITY UPLC BEH C18 1.7 μm (φ2.1 × 50 mm), and 10 μL samples were injected. The eluent was A: 0.1% formic acid and B: acetonitrile, and the ratio of acetonitrile was raised from 1% to 35% in 8 min with a linear gradient at the flow rate of 0.5 mL/min. Ionization mode for mass spectrometry was ES+, and *m/z* 540-990 was scanned in full scan mode. Other mass parameters were as follows: capillary; 2.5 kV, cone; 30 V, source temperature; 150°C, dessolvation temperature; 650°C, cone gas flow; 150 L/h, and dessolvation gas flow; 1000 L/hr.

Assessment of the *in vivo* repair rate of UV-induced 6-4PPs

Cells were cultured to 90% confluence in a 96-well glass bottom plates (Matsunami Glass). After removal of the culture medium, the cells were irradiated with UVC at 10 J/m^2 and cultured in fresh medium for various times to allow repair of the photolesions. The culture medium was then removed, and the cells were fixed for 10 min at room temperature with 2% paraformaldehyde in PBS. To serve as standards for quantification, cells in separate wells were exposed to different doses of UVC (0, 5, and 10 J/m^2) and fixed immediately.

Immunostaining of UV-induced 6-4PPs was carried out essentially as described previously (Okuda et al., 2015). The Alexa Fluor 405-labeled anti-mouse IgG secondary antibody was used to visualize 6-4PPs, and nuclear DNA was counterstained for 20 min at room temperature with 1 μg/mL propidium iodide (PI). Fluorescent images were acquired with the confocal laser scanning microscope, and the fluorescence intensities for 6-4PPs and genomic DNA in individual cell nuclei were measured with the MATLAB software. As there was a linear correlation between the levels of 6-4PPs and nuclear DNA (Figure S11), Alexa Fluor 405 fluorescence (6-4PP) was divided by PI fluorescence (DNA) to obtain the relative 6-4PP level for each nucleus. Median values were used to draw a standard curve and calculate the relative 6-4PP level in samples.

QUANTIFICATION AND STATISTICAL ANALYSIS

Statistical analyses were performed using GraphPad Prism 9. Statistical parameters and tests are reported in the figures and corresponding figure legends. To assess statistical difference, parametric tests (two-tailed Student's *t* test for comparison of two samples, one-way ANOVA followed by Tukey's HSD test for comparison of three or more samples) were used for most assays, where the Gaussian normality and comparable variance of data could be assumed. In each plot graph, the mean value with 95% confidence interval is shown. For other assays (such as LacO-LacR tethering assay and correlation coefficient analysis), non-parametric tests (Mann-Whitney U test for comparison of two samples, Kruskal-Wallis test followed by Dunnet's test for comparison of three or more samples) were chosen, so that the median with 95% confidence interval is shown in a plot graph. To assess enrichment of MTAs and HDACs (Figures 2B and S6A) or reduction of H3K27ac (Figures S5D and S8B) at LUD sites or *lacO* arrays, one sample *t*-tests (two tailed) were also applied.